CHAPTER 6

New Concepts in Photocatalysis

YING WU[a,b] AND MICHAEL WARK*[a]

[a]Institute of Chemistry, Technical Chemistry, Carl von Ossietzky University Oldenburg, Carl-von-Ossietzky-Str. 9-11, 26129 Oldenburg, Germany; [b]Institute of Physical Chemistry, Zhejiang Key Laboratory for Reactive Chemistry on Solid Surfaces, Zhejiang Normal University, Jinhua 321004, China
*E-mail: michael.wark@uni-oldenburg.de

6.1 Introduction

In the twenty-first century, aggravating energy and environmental problems such as pollution, fossil fuel depletion, and global warming are ringing the alarm bells for human society. Photocatalysis and photoelectrochemical processes have attracted much attention in recent decades because of their potential for environmental purification and converting solar photo energy into chemical energy. These green technologies have been extensively applied to nonselective degradation processes of pollutants, selective organic conversion for synthesis of fine chemicals and water splitting for the formation of hydrogen as energy storage gas. However, the practical applications of these techniques are limited by the ineffective utilization of visible light, insufficient quantum efficiency, or the possible photocorrosion of the catalyst. Therefore, it is desirable and urgent to design novel catalysts with high photocatalytic and/or photoelectrochemical efficiency. In recent years, numerous novel photocatalysts have been engineered and applied, such as g-C_3N_4 and graphene-based composites. They exhibit good photocatalytic performance due to unique properties and/or special mechanisms.

RSC Energy and Environment Series No. 14
Photocatalysis: Fundamentals and Perspectives
Edited by Jenny Schneider, Detlef Bahnemann, Jinhua Ye, Gianluca Li Puma, and Dionysios D. Dionysiou

Published by the Royal Society of Chemistry, www.rsc.org

This chapter gives a brief overview of the promising photocatalytic materials/systems currently used mainly for water splitting and degradation of pollutants as well as some new applications in photocatalysis. We describe the most recent improvements in this area, also referring to papers published earlier, to provide an updated overview of the photocatalyst features needed for photocatalytic reactions. The focus is mainly on new photocatalytic systems and applications in photocatalysis.

6.2 Graphene

Dating back to October 2004, a revolution in science and technology was triggered by the report that Geim and Novoselov had prepared two-dimensional sheets of carbon atoms – graphene (GR).[1] Graphene is regarded as an ideal high performance candidate for photocatalyst carriers or promoter and has attracted a lot of attention due to its outstanding mechanical, thermal, optical transmittance (~97%), and thermal conductivity (~5000 $W\ m^{-1}\ K^{-1}$). It offers an excellent mobility of charge carriers at room temperature (200 000 $cm^2\ V^{-1}\ s^{-1}$), and exhibits an extremely high theoretical specific surface area (~2630 $m^2\ g^{-1}$).[2–4]

Graphene, as an allotrope of carbon, is composed of sp^2-bonded carbon atom layers packed into a honeycomb network that can be exfoliated from bulk graphite using different approaches, including "bottom-up" and "top-down" methods. In the bottom-up methods graphene is synthesized from atoms or molecules *via* chemical reactions, for instance, epitaxial growth on single-crystal SiC and chemical vapor deposition on metal foil surfaces.[5–7] In comparison, the top-down methods are more often used because of their convenience and lower cost. To date, high-quality graphene with a well-defined molecular structure is usually prepared by top-down methods such as chemical exfoliation of graphite, thermal exfoliation and electrostatic deposition. The most widely used technique is the chemical reduction of graphene oxide (GO) as shown in Figure 6.1,[8] which is usually conducted by Hummers' method.[9] In this method the reduced GO product is purified by centrifugation, washing, and dialysis to remove aggregates and various inorganic impurities such as residual ions and acids. The exfoliated GO sheets usually possess a rich assortment of oxygen-containing groups, such as carboxylic, hydroxyl, and epoxide functional groups. The oxygen functionalities in GO can interact with the cations and provide reactive sites for the nucleation and growth of nanoparticles, which leads to the rapid growth of various graphene-based composites. Moreover, the functional GO can be reduced to graphene with partial restoration of the sp^2-hybridized network by thermal, chemical, electrochemical, photothermal, photocatalytic, sonochemical, and microwave reduction methods.

The graphene-based composites can be synthesized by various preparation methods. The direct *in situ* growth strategy is widely used to prepare graphene-metal composites by using functional GO and metal salts as precursors. This *in situ* procedure can avoid the agglomeration of the

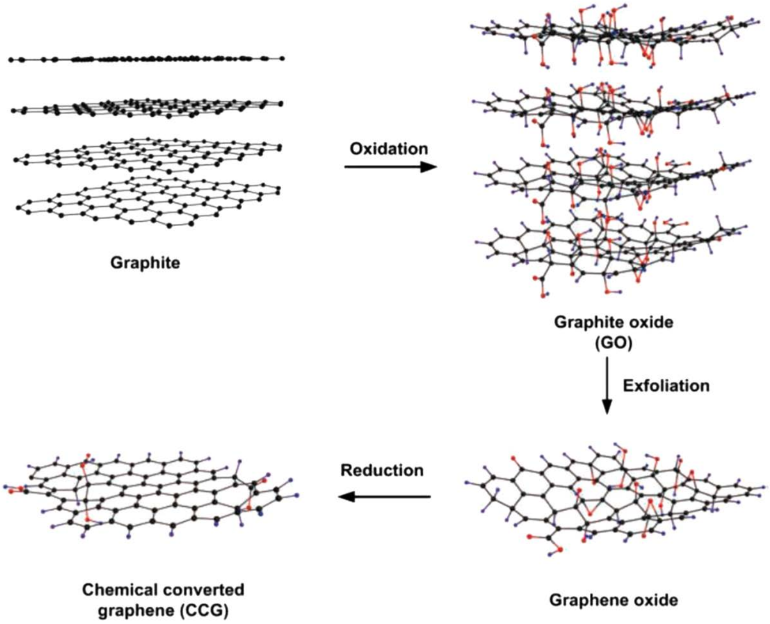

Figure 6.1 Preparation of graphene by chemical reduction of graphene oxide synthesized by Hummers' method. (Reprinted with permission from ref. 8. Copyright 2011 John Wiley & Sons.)

semiconductor nanoparticles on the graphene sheets. The solution mixing method has been broadly used to fabricate graphene-semiconductor composite photocatalysts. Through this process GO can also hybridize with other graphite-like materials by forming strong π–π bonds. Another effective way for preparing graphene-semiconductor composite is the hydrothermal/solvothermal process, by which semiconductor nanoparticles or their precursors are loaded on the graphene oxide sheets, followed by reduction to graphene.

GR-based photocatalysts prepared by various methods have been extensively used for the degradation of pollutants, disinfection, and hydrogen generation. Zhang *et al.*[10] have prepared a chemically bonded TiO_2 (P25)-GR nanocomposite *via* a facile one-step hydrothermal method using GO and P25 as the precursors. As shown in Figure 6.2 the introduction of graphene caused a bandgap narrowing of P25, resulting in a significant enhancement of the activity towards the photodegradation of methylene blue (MB) in water under both UV and visible light irradiation.[11] The supposed degradation process was that MB molecules can be transferred from the solution to the surface of TiO_2 where they adsorb with offset face-to-face orientation *via* π–π conjugation between MB and aromatic regions of graphene. This leads to an increased adsorption of dyes compared to bare P25. Moreover, the TiO_2 (P25)-GR nanocomposite also shows a higher photodegradation rate than P25-carbon nanotube (CNT) composites with the same carbon content,

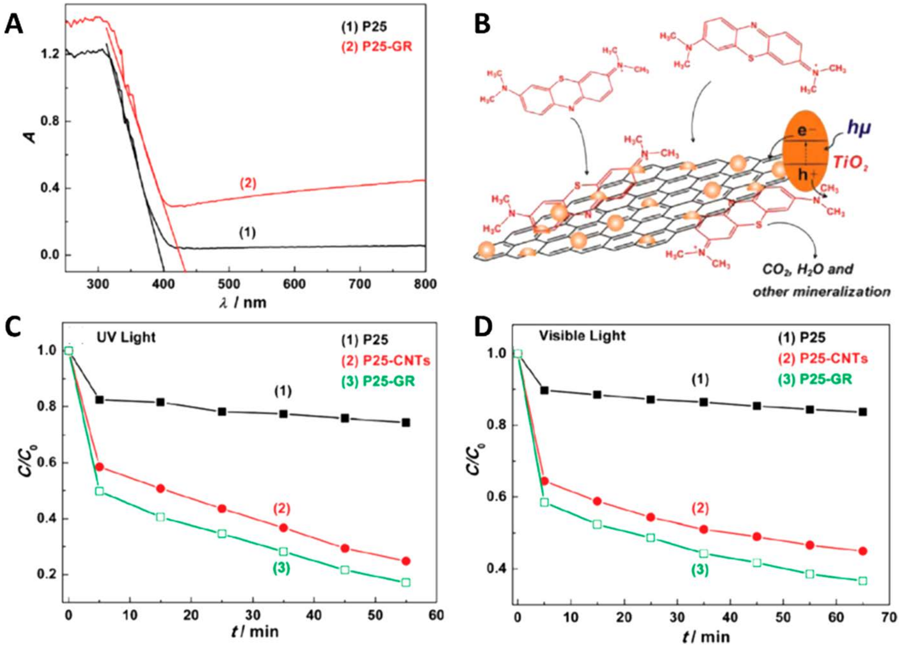

Figure 6.2 (A) Diffuse reflectance absorption spectra of P25-graphene; (B) schematic structure of P25-graphene and tentative processes of the photodegradation of MB (methylene blue) over P25-GR; comparison of photocatalytic activity in the degradation of MB under (C) UV light (365 nm) and (D) visible light ($\lambda > 400$ nm) over (1) P25, (2) P25-CNTs, and (3) P25-graphene photocatalysts. (Reprinted with permission from ref. 10. Copyright 2010 American Chemical Society.)

which is mainly ascribed to the giant two-dimensional planar structure, the improvement of the dye adsorption, and the enhancement of charge carrier transportation due to the addition of graphene. This work opens new possibilities in the application of TiO_2–carbon composites as photocatalysts for water purification. Apart from TiO_2–graphene, composites of graphene and other semiconductors such as MoS_2–GR–TiO_2, SnO_2–GR, $ZnFe_2O_4$–GR, Bi_2WO_6–GR, BiOI–GR, $SmVO_4$–GR, Ag_2CO_3–GR, and Ag–C_3N_4–GR have been reported as efficient photocatalysts for decomposition of pollutants in water.[12–19]

Graphene-based composites can also be used for water splitting. As oxygen bonds with GR, the valence band changes from the p-orbital of GR to the O 2p orbital, leading to a larger band gap for higher oxidation levels of GO. Yeh *et al.*[20] researched the electronic band energy levels of GO with various oxidation levels. The results reflect that, with sufficient oxidation, the electronic structure of GO is suitable for both the reduction and oxidation of water under illumination, and the production of H_2 and O_2 in the presence of sacrificial reagents. Zhang *et al.*[21] studied the water splitting performance of TiO_2-graphene with different graphene content. Under Xe lamp irradiation and using Na_2S and Na_2SO_3 as sacrificial agents, a H_2 production rate of 8.6 μmol h^{-1} can be obtained on TiO_2-5.0 wt% graphene catalyst, exceeding the rate on pure P25 by more than two times. The enhanced photocatalytic H_2 production activity was attributed to the role of graphene sheets as electron acceptors to efficiently separate the photogenerated charge carriers. Fan *et al.*[22] systematically studied the efficiency of H_2 evolution for TiO_2 (P25)-graphene composites synthesized by UV-assisted photocatalytic reduction, hydrazine reduction, and hydrothermal methods. All the composites prepared by different methods exhibited better photocatalytic performance for H_2 evolution from methanol aqueous solution than bare P25. Therein, the P25-graphene composite prepared by the hydrothermal method affords the highest rate of H_2 evolution, which is also higher than that over P25-CNT prepared by the same method. Iwase *et al.*[23] has developed an ingenious Z-scheme photocatalysis system for water splitting under visible light irradiation. Mixtures of photoreduced graphene oxide (PRGO) with $BiVO_4$ (PRGO/$BiVO_4$) and Ru/$SrTiO_3$: Rh (PRGO/Ru/$SrTiO_3$: Rh) are prepared by photocatalytic reduction of GO on $BiVO_4$ and Ru/$SrTiO_3$: Ru, respectively, under visible light illumination in the presence of methanol as a hole scavenger. In the photocatalyst, PRGO functions as a solid-state electron mediator, transferring the electrons from the conduction band of $BiVO_4$ to vacancies in the impurity level of Ru/$SrTiO_3$: Rh. The electrons in Ru/$SrTiO_3$: Rh reduce water to H_2 on the Ru co-catalyst, while the holes in $BiVO_4$ oxidize water to O_2, accomplishing a complete water splitting cycle. The time courses of H_2 and O_2 evolution indicates that this system is stable for at least two cycles studied.

Graphene-based composites may potentially be used in other domains as well. Akhavan *et al.*[24] found that graphene–TiO_2 films prepared *via* deposition of graphene oxide platelets on TiO_2 thin films followed by annealing and irradiation process were able to destroy more than 99.9% of *Escherichia coli* bacteria in an aqueous solution under solar light irradiation. Its antibacterial activity is improved by about 6 and 7.5 times related to the activity of the annealed GO–TiO_2 and the bare TiO_2 thin film, respectively. Furthermore, the graphene platelets were chemically stable after photoinactivation of the bacteria. Similarly, graphene–WO_3 thin films also show an excellent visible light photocatalytic performance in the photoinactivation of viruses.[25] A new heteroleptic ruthenium complex containing 2-thiophenylbenzimidazole ligands was immobilized to graphene oxide *via* covalent attachment and used for the photoreduction of carbon dioxide under visible light irradiation without using a sacrificial agent. It gave 2050 μmol g^{-1} methanol after 24 h of irradiation, which is four-times higher than for bare GR.[26] Au/Fe_2O_3–GO nanocomposites prepared by a one-pot hydrothermal synthesis approach followed by noble precursor injection exhibited high catalytic activity and recyclability for the reduction of 4-nitrophenol.[27] In addition, graphene quantum dots (GRQDs) that were prepared by Zhuo *et al.*[28] *via* a facile ultrasonic route exhibit an extraordinary excitation-independent photoluminescent (PL) behavior. Based on the upconversion PL properties of GRQDs, rutile/anatase TiO_2/GRQD complex photocatalysts were designed to harness the visible spectrum of sunlight and used in the degradation of methylene blue. The results show that the photocatalytic rate of the rutile TiO_2/GRQD complex system is *ca.* nine times larger than that of the anatase TiO_2/GRQD complex under visible light (λ > 420 nm) irradiation. These studies opened a new doorway for the use of graphene in the design of highly efficient systems.

Coupling graphene with suitable semiconductor and metal nanostructures is one of the most promising ways to design photocatalyst systems. Although exciting developments have already obtained, great opportunities still exist for the formation of novel graphene-based hybrid materials. Due to the high dependency of the photocatalyst properties on the surface structure, the structural evolution of loaded nanomaterials should be intensified by controlling their morphologies, phase structures, porosities, surface active sites, *etc.* Meanwhile, the underlying mechanism of the enhanced photocatalytic activity by graphene-based assembly is not fully understood. In general, the performance enhancement of graphene-based photocatalysts is ascribed to the extended absorption and improved charge transfer in the hybrids. Thorough research on the interfacial chemistry of the photocatalysts is important and necessary to clarify the possible mechanism of the photocatalytic reaction. Moreover, the structure of graphene sheets in the composites should be noted because of its tunable optical and electronic properties. The engineering of highly effective graphene-based composites is very challenging due to the existence of defects or oxidation sites in the partially-restored graphene.

6.3 Carbon Nitride

Graphitic carbon nitride (g-C_3N_4) is another novel material with a two-dimensional (2D) structure. Lately, it has drawn considerable attention in catalysis as it shows interesting photochemical properties and the physicochemical features that make it an ideal choice both as a metal-free catalyst and as a catalyst support. Although g-C_3N_4 has a long history, the potential value of this material was not fully recognized until recent decades, due to its chemical inertness, insolubility in acidic, neutral or basic solvents, and its unrevealed structure. The study of C_3N_4 started in 1834 when Berzelius and Liebig made a polymeric derivative and named it "melon".[29] It was followed by many theoretical studies until g-C_3N_4 was demonstrated to be the most stable allotrope of carbon nitride under ambient conditions. Since then, more research has focused on the structure and composition study of g-C_3N_4 materials. Inspired by the structure of graphite, triazine (C_3N_3) had been put forward as the elementary building block of g-C_3N_4 (Figure 6.3a).[30] However, another possible building block, tri-*s*-triazine (heptazine) rings, which are structurally related to the hypothetical polymer melon, have recently shown to be energetically favored with respect to the triazine-based modification

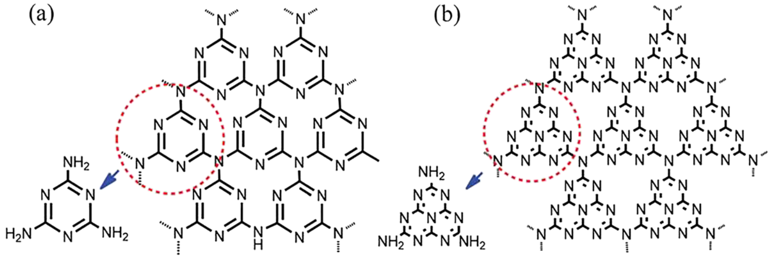

Figure 6.3 Structures of *s*-triazine (a) and tri-*s*-triazine (b) as tectons of g-C_3N_4. (Reproduced from ref. 30 with permission from The Royal Society of Chemistry.)

(Figure 6.3b). The tri-*s*-triazine rings are crosslinked by trigonal nitrogen atoms, and a recent work has shown that indeed the pyrolysis of cyanamide, dicyandiamide, or melamine yields a melon polymer built up from melem units, confirming that this tecton is the most stable local connection pattern.[31]

The ideal g-C_3N_4 consists solely of an assembly of C–N bonds without electron localization in the π state. However, the existing g-C_3N_4 contains a small amount of hydrogen, present as primary and/or secondary amine groups on the terminating edges. The existence of hydrogen suggests that the real g-C_3N_4 is incompletely condensed with a number of surface defects. Such defects are believed to promote electron relocalization on the surface, inducing Lewis-base character toward metal-free coordination chemistry and catalysis. Meanwhile, the presence of hydrogen and nitrogen means that g-C_3N_4 possesses rich surface properties, such as, for example, basic surface functionalities, electron-rich properties, and H-bonding motifs. Moreover, its high thermal (up to 600 °C in air) and chemical stability (against acids, bases, and organic solvents) enables g-C_3N_4 to function either in liquid or gaseous environments as well as at elevated temperatures, which potentiates its widespread application in heterogeneous catalysis. Despite the similar microstructure, graphite and g-C_3N_4 present entirely different physicochemical properties. Besides the diverse appearance (g-C_3N_4: yellow; graphite: black), the electronic properties of the two materials are thoroughly different. Graphite reveals excellent conductivity in the dimensions of the layers, whereas g-C_3N_4 is characterized as a wide-band semiconductor. Therefore, g-C_3N_4 is a promising alternative candidate for photosensitive catalysts.

The application of polymeric g-C_3N_4 to photocatalysis was first reported by Wang *et al.*[32] in 2009 and great achievements on the photocatalytic behavior and its reaction mechanism have been obtained since. In contrast with traditional inorganic metal catalysts, the metal-free material g-C_3N_4 has high chemical stability and can be tailored as desired due to its polymeric properties, rendering it a promising photocatalyst. However, the photocatalytic efficiency of g-C_3N_4 is still restricted due to the large optical band gap and the fast recombination rate of photogenerated electron–hole pairs. To improve its photocatalytic behavior, a few ways have been attempted. The visible light photocatalytic performance of g-C_3N_4 can be greatly enhanced by structured design, band gap engineering, dye sensitization, and heterojunction construction.[33]

Water splitting using a photocatalytic process under visible-light irradiation is the "holy grail" to produce hydrogen fuel because the process can convert sunlight into storable and transportable energy in chemical bonds. g-C_3N_4 can provide all the prerequisites required for water splitting by heterogeneous photocatalysis owing to its structural and electronic properties. It is identified as a visible-light-responsive polymeric semiconductor with a band gap of ~2.7 eV, corresponding to an optical wavelength of ~460 nm. The band gap is sufficiently large to overcome the endothermic character of the water-splitting reaction. The band potentials are appropriate for both water reduction and oxidation. Moreover, g-C_3N_4 exhibits an appropriate microstructure, with surface termination with defects and nitrogen atoms for electron localization or for anchoring the active sites. The bare g-C_3N_4 catalyst exhibits activities for water reduction into H_2 or water oxidation into O_2 in the presence of an appropriate sacrificial electron donor or acceptor.

Because g-C_3N_4 has a similar layered structure as graphite, the specific surface area could theoretically be increased up to 2500 $m^2\ g^{-1}$ for perfect monolayer g-C_3N_4, whereas normally it is below 10 $m^2\ g^{-1}$ for bulk g-C_3N_4 due to the stacking of polymeric nanosheets. Control of the g-C_3N_4 structure can endow it with a large surface area, abundant surface states, and even extended light harvesting. Nanosheets of g-C_3N_4 exfoliated in 2-propanol by sonication with a surface area of 384 $m^2\ g^{-1}$ show a nine-times higher hydrogen evolution rate than bulk C_3N_4 under visible light irradiation.[34] The morphology modulation of g-C_3N_4 is another way to enhance the photocatalytic performance by facilitating the light absorption, charge separation and migration, and mass diffusion during photocatalytic reactions. The efficiency of hydrogen production by the photochemical reduction of water can be improved eight-fold through the introduction of mesopores into g-C_3N_4.[35] Heteroatom doping and the introduction of other organic additives can also effectively manipulate the electronic band structure of g-C_3N_4 to extend the light absorption and adjust the redox potential to further promote the photocatalytic activity. Doping sulfur into carbon nitride leads to a downshift of 0.25 eV in the conduction band and shows extended and stronger visible-light absorption and a much lower density of defects, and thus exhibits 30-times higher H_2 evolution activity, compared to that of mesoporous C_3N_4 (mpg-C_3N_4).[36] Oxygen- or fluorine-doped g-C_3N_4 also shows a significant improvement in the evolution of H_2 under visible light irradiation.[37,38] The incorporation of carbon nanodots (CDots) into the g-C_3N_4 matrix can lead to an increase in the ultraviolet visible absorption, and thus CDots–g-C_3N_4 exhibits impressive stability and performance for photocatalytic solar water splitting, with quantum efficiencies of 16% for wavelengths of $\lambda = 420 \pm 20$ nm and 6.29% for $\lambda = 580 \pm 15$ nm, as well as an overall solar energy conversion efficiency of 2.0%.[39] The incorporation of metal ions into the framework of g-C_3N_4 can strongly modify the electronic properties of g-C_3N_4 and affords additional functionalities for the materials. As an organic polymeric semiconductor, g-C_3N_4 can develop delocalized electron states, as the metal particles and g-C_3N_4 are not independent. The work functions of most noble metals are located between the conduction band and valence band of g-C_3N_4. Metal particles with higher work function can give an elevated Schottky barrier, and thus enhance charge separation at the interface of the metal–semiconductor heterojunction, which has a great impact on the performance of photocatalysts. In fact, g-C_3N_4 would not only be just a metal carrier but also an "active support" that promotes the catalytic activity or selectivity of the metal particles. Although the detailed formation mechanism is not yet fully understood, transition metal ions (*e.g.* Fe^{3+}, Zn^{2+}) can be incorporated into the framework of g-C_3N_4 to form an organic–inorganic hybrid material.[40] The deposit of noble metals (*e.g.* Pt, Rh) promotes the reaction, not only by modifying the electronic properties of the material but also by interacting with the intermediate as a co-catalyst.[41] Another effective strategy to populate the conduction band of g-C_3N_4 with abundant electrons is coupling with suitable organic dyes, the excitation of which enables the energy conversion of light at longer wavelengths. In this strategy, the dyes act as antennas to absorb and transfer the light energy into the reaction system. Semiconductor hybridization is another effective strategy to decrease the recombination rate of photoinduced electron–hole pairs. Both inorganic metal semiconductors and organic or polymer materials can be used to hybridize with g-C_3N_4, although they play different roles in the reaction. Enhanced photocatalytic activities of g-C_3N_4/metal (hydr)oxide or g-C_3N_4/metal sulfide nanocomposites have been reported.[42] The geometric similarity of layered MoS_2 or WS_2 and g-C_3N_4 facilitates the formation of intimate planar interfaces, which can significantly promote the photo-activity of MoS_2/g-C_3N_4 or WS_2/g-C_3N_4 (Figure 6.4).[43] They even exhibit higher photocatalytic visible-light performance of H_2 production than Pt/mpg-C_3N_4. Polymer materials, graphene and graphitized polyacrylonitrile (g-PAN), can also be introduced to strengthen H_2 generation by acting as conductive channels,

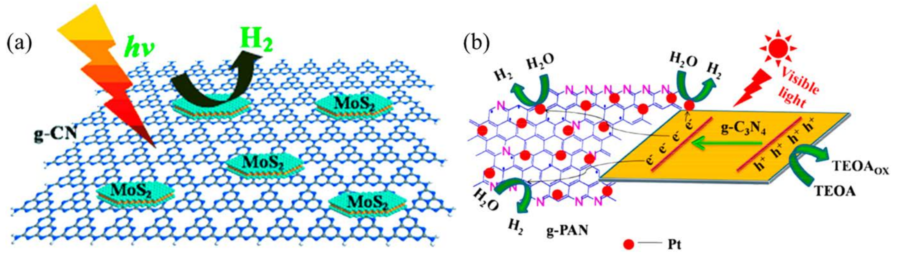

Figure 6.4 Schematic diagram showing the process of H_2 evolution reaction over (a) MoS_2/mpg-C_3N_4 layered junctions, (b) g-PAN/g-C_3N_4 composites under visible light irradiation (PAN, polyacrylonitrile). ((a) Reprinted with permission from ref. 43. Copyright 2012 John Wiley & Sons. (b) Reprinted with permission from ref. 44. Copyright 2014 American Chemical Society.)

efficiently separating the photogenerated charge carriers, as well as enhancing the visible-light capability of H_2-production.[44]

In recent years, great effort has been devoted to solve the widespread pollution of effluents and gaseous pollutants from urban and agricultural industries. Various catalytic techniques have been applied in environmental conservation. Photocatalysis has been widely used in environmental applications such as air purification, water disinfection, hazardous water remediation, and water decontamination. The g-C_3N_4-based semiconductor photocatalysts exhibit high dye adsorption capacity, extended light absorption boundary, and accelerated charge transportation and separation properties. Yan *et al.*[45] found that g-C_3N_4 was able to degrade methyl orange (MO) and Rhodamine B (RhB) as a metal-free photocatalyst. Comparison studies showed that the activity for the photodegradation of MO over g-C_3N_4 is attributed mainly to the reduction process initiated by photogenerated electrons, whereas the degradation of RhB originates primarily from oxidation by the photogenerated holes. The doping of boron into g-C_3N_4 can improve the dye adsorption and light absorption, and therefore promote the photodegradation of RhB. TaON can couple with g-C_3N_4 due to a suitable matching with conduction and valence band levels, and can, thus, improve the separation efficiency of photogenerated electron–hole pairs. Similarly, the incorporation of WO_3 into g-C_3N_4 contributed to the superior photocatalytic reactivity by hampering the recombination of the photo-generated electrons and holes.[46] The WO_3/g-C_3N_4 heterojunction can also be used to remove the poisonous gaseous pollutant acetaldehyde (CH_3CHO), which is a typical volatile organic compound (VOC) and exerts adverse effects on the health of humans.[47] In addition, g-C_3N_4/TiO_2, Fe_2O_3/g-C_3N_4, ZrO_2/g-C_3N_4, $BiVO_4$/g-C_3N_4, BiOCl/g-C_3N_4, $LaVO_4$/g-C_3N_4, $SmVO_4$/g-C_3N_4, Zn_2SnO_4/g-C_3N_4, Ag_2CO_3/g-C_3N_4, P/g-C_3N_4, and Pd/g-C_3N_4 have been reported as efficient photocatalysts for decomposition of pollutants in water.[48–59] In the same way, g-C_3N_4-based heterojunctions can contribute to the degradation of nitric oxides NO_x, which have been regarded as a worldwide important gaseous pollutant.[60] The g-C_3N_4/BiOBr and g-C_3N_4/g-C_3N_4 isotype heterojunctions exhibit higher NO_x removal degrees than pristine g-C_3N_4, which can be directly ascribed to the effectively accelerated charge separation across the heterojunction interface.[61]

As a “rising star”, g-C_3N_4 has been extensively applied to photocatalytic reactions due to its exceptional properties. Although much significant progress has been achieved in the photocatalysis domain, further efforts are still required in various aspects to improve the utilization of g-C_3N_4. Due to its surface properties g-C_3N_4 is relatively inert compared with graphene, which usually possesses many oxygen-containing groups; in-depth studies are needed on the surface activation of g-C_3N_4 for the purpose of specific binding of functional groups, as well as the growth and well dispersion of nanoparticles. It is beneficial to prepare more efficient g-C_3N_4/semiconductor heterojunction or hybrids with improved interfacial contact for a photocatalytic reaction. In addition, although the energy band engineering of g-C_3N_4 has been widely applied, high quantum efficiency cannot be achieved by simply tuning the band gap to extend light absorption. Therefore, the combination of band gap engineering with other modification strategies is highly encouraged to find more efficient ways to promote the performance of g-C_3N_4. Furthermore, the mechanisms of g-C_3N_4-based photocatalytic systems are not yet very clear. It is necessary to understand the dynamic behavior of photogenerated carriers on the surface and interface of g-C_3N_4 with reactants.

6.4 Z-Scheme Photocatalytic Systems

The term "Z-scheme", originating from its shape, has been used to interpret the mechanism of natural photosynthesis by green plants in which two chlorophyll molecules, P700 and P680 (photosystem I and II), harvest 700 and 680 nm photons, respectively. The photosystem can oxidize H_2O into O_2 under sunlight, with a quantum yield close to unity. The natural Z-scheme photocatalytic process involves a two-step photoexcitation (Figure 6.5).[62] First, the electrons in the highest occupied molecular orbital (HOMO) of an oxygen-evolving complex labeled as photosystem II (PSII) are excited to its lowest unoccupied molecular orbital (LUMO) under solar light. Then the photogenerated electrons in LUMO of PSII are transferred to HOMO of ferrodoxin–NAPD reductase labeled as photosystem I (PSI) through the electron mediator. Further, the electrons in HOMO of PSI are excited to its LUMO. As a result, photogenerated electrons and holes are left in the LUMO of PSI and the HOMO of PSII, respectively. This process is different from the conventional heterojunction-type charge transfer mechanism. Finally, the photogenerated electrons in the LUMO of PSI are used to reduce CO_2, while the

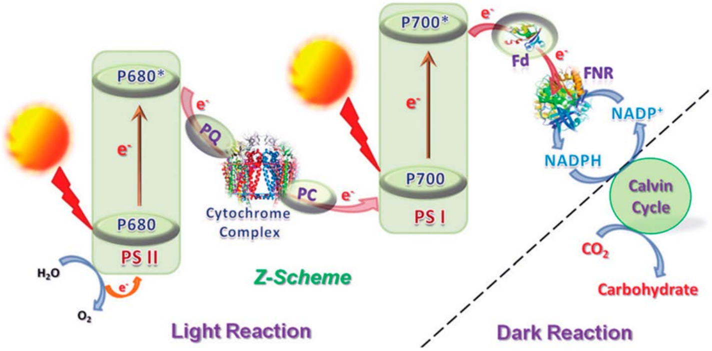

Figure 6.5 Simplified schematic representation of natural photosynthesis in green plants. Photoexcited electrons, on being transferred *via* a series of electron transfer chain reactions (in both PSII and PSI), are eventually utilized to reduce the coenzyme $NADP^+$ in the presence of a redox enzyme, FNR (in PSI). Regenerated cofactor NADPH is subsequently used up in the Calvin cycle for the production of carbohydrate from CO_2. PQ = plastoquinone, PC = plastocyanin, Fd = ferredoxin, FNR = ferredoxin $NADP^+$-reductase. (Reproduced from ref. 62 with permission from The Royal Society of Chemistry.)

photogenerated holes in the HOMO of PSII are used to oxidize H_2O. Thus, the Z-scheme photocatalytic system shows the strong reducibility of PSI and the strong oxidizability of PSII. Therefore, excellent redox ability can potentially be achieved in a Z-scheme photocatalytic system which may consist of two narrow-bandgap semiconductors exhibiting excellent absorption of visible light. In view of the unique advantages of the natural Z-scheme photocatalytic system, artificial Z-scheme photocatalytic systems have been widely designed and investigated over the past three decades, leading to tremendous developments in this exciting research area.

In an artificial Z-scheme photocatalytic system, two different photocatalysts are combined using an appropriate shuttle redox mediator. In this way, visible light can be utilized more efficiently than in the conventional one-step water-splitting systems because the energy required to drive each photocatalyst is reduced. It is also possible to apply a photocatalyst that has either water reduction or oxidation potential to one side of the system. Based on the type of the employed electron mediators, the Z-scheme photocatalytic systems can be divided into liquid-phase Z-scheme systems with redox mediator and solid-state Z-scheme systems without redox mediator. They exhibit the obvious differences in the preparation methodology, working mechanism, properties, and applications. Although historically Z-scheme photocatalytic systems were mostly used for water splitting, in recent years more attention has been paid to the exploration of Z-scheme systems for the degradation of pollutants and for CO_2 reduction.

6.4.1 Z-Scheme Systems with Redox Mediator

In the Z-scheme systems with redox mediator (labeled as PS–A/D–PS), the electron acceptor/donor (A/D) pair is a common electron mediator. Such a photocatalytic system can only work in liquid-phase due to limitations of the A/D pair. As shown in Figure 6.6,[63] photocatalytic systems with two separate

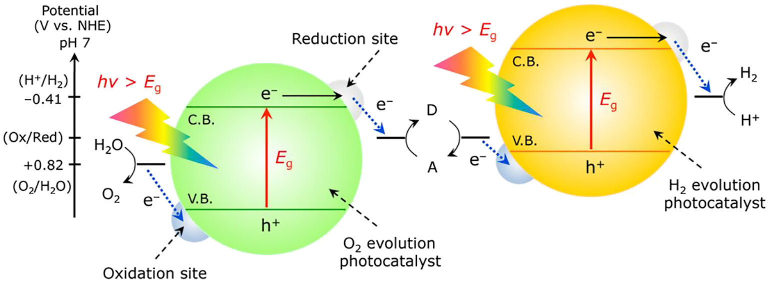

Figure 6.6 Schematic energy diagram of photocatalytic water splitting for a two-step photoexcitation system. CB: conduction band; VB: valence band; E_g: band gap; D and A indicate electron donating and accepting species, respectively. (Reprinted with permission from ref. 63. Copyright 2013 American Chemical Society.)

semiconductors based on an indirect Z-scheme mechanism using reversible redox mediators such as Fe^{3+}/Fe^{2+} have been successfully designed for the overall water splitting into H_2 and O_2. The first demonstration of stoichiometric H_2 and O_2 evolution *via* Z-scheme water splitting was accomplished by Sayama *et al.* in 1997.[64] They coupled RuO_2-loaded WO_3, which operates water oxidation in the presence of Fe^{3+} ions, with a photochemical H_2 evolution system involving Fe^{2+} ions. Under ultraviolet (UV) irradiation ($\lambda > 200$ nm), H_2 evolution occurs photochemically through excitation of Fe^{2+} by UV light, followed by photochemical reduction of water and the generation of Fe^{3+}, while the RuO_2/WO_3 photocatalyzes water oxidation using Fe^{3+} as an electron acceptor. It was also demonstrated that this system could produce H_2 and O_2 separately. Only H_2 was evolved from an aqueous $FeSO_4$ solution without any photocatalyst powder under UV irradiation ($\lambda > 200$ nm), whereas only O_2 evolution occurred from the same reactant solution after addition of RuO_2/WO_3 powder under $\lambda > 300$ nm irradiation. The IO_3^-/I^- pair is another common redox mediator. In 2001, Abe *et al.*[65] succeeded in a two-step water splitting using a system consisting of Pt/anatase TiO_2 and rutile TiO_2 as H_2 and O_2 evolution photocatalyst, respectively, under UV irradiation ($\lambda > 300$ nm) in the presence of IO_3^-/I^- redox mediator. The water-splitting reaction involving an IO_3^-/I^- redox couple was initiated by photo-oxidation of I^- into IO_3^- and photoreduction of H^+ into H_2 on a H_2 evolution photocatalyst, after which photoreduction of IO_3^- into I^- and photo-oxidation of H_2O into O_2 occurred on the O_2 evolution photocatalyst. Apart from oxides, (oxy)nitrides – which are interesting compounds because of their light-harvesting properties and band-edge positions suitable for both water reduction and oxidation – can also be used to construct Z-scheme water splitting systems. In 2005, Abe *et al.*[66] applied Pt-loaded TaON as a Z-scheme water-splitting photocatalytic system for H_2 evolution. Pt/TaON produced H_2 from an aqueous solution containing NaI as an electron donor under visible light, although the rate of H_2 evolution decreased with reaction time. This deactivation is ascribed to the backward reaction (photoreduction of IO_3^- by photogenerated electrons), which takes place in the conduction band of the catalyst, as also observed for other H_2 evolution photocatalysts. The fact that neither O_2 nor N_2 was produced during the reaction process indicated that photogenerated holes in the valence band of TaON efficiently oxidized I^- into IO_3^-, which is consistent with the results of photoelectrochemical analyses for TaON electrodes. The combination of Pt/TaON[67] and PtO_x/WO_3[68] with an IO_3^-/I^- redox mediator resulted in stoichiometric water splitting into H_2 and O_2 under visible light, with an atomic quantum yield (AQY) of 0.5% at 420 nm. The water-splitting behavior was stable at pH 5.3, producing stoichiometric H_2 and O_2 during 60 h of reaction. With modification by Ru co-catalysts, TaON also functioned as a building block for O_2 evolution in Z-scheme water splitting in the presence of the IO_3^-/I^- redox couple.

The redox mediators are, in principle, indispensable and play vital roles in achieving Z-scheme water splitting, but can cause several kinds of undesirable backward reactions, which lead to a sharp decrease in the effective number of photogenerated electrons and holes. Furthermore, the often used A/D pairs, such as IO^{3-}/I^-, Fe^{3+}/Fe^{2+}, $[Co(bpy)_3]^{3+}/[Co(bpy)_3]^{2+}$, $[Co(phen)_3]^{3+}/[Co(phen)_3]^{2+}$, and NO_3^-/NO_2^-,[69] absorb light to different extents, which decreases the number of photons absorbed by the photocatalyst. Beyond that, in most cases these A/D pairs lack long-term stability over a wide range of pH, which lessens the number of suitable A/D pairs. Consequently, the Z-scheme electron transfer rate between H_2 and O_2 evolution photocatalyst will be slowed down. Hence, a Z-scheme water splitting system that does not rely on any redox mediator is highly desirable.

6.4.2 Z-Scheme Systems Without Redox Mediator

A photocatalytic material with a built-in electric field at the interface of p- and n-type semiconductor might be an ideal redox mediator-free system. A solid-state Z-scheme photocatalytic system without redox pairs is constructed by employing a conductor (C) as the electron mediator between the artificial photosystems, *i.e.* the H_2 and O_2 evolution photocatalyst (labeled as PS–C–PS), or a direct solid–solid contact interface between the photosystems (labeled as PS–PS).[70]

The Z-scheme anisotropic TiO_2–Au–CdS photocatalytic system reported in 2006 is the first example of a solid-state PS–C–PS system.[71] It was constructed by the photochemical deposition–precipitation method and exhibited higher photocatalytic activity than both the two-component Au–TiO_2 and TiO_2–CdS systems, which was ascribed to the presence of Au nanoparticles with a dimension of 3.4 nm between TiO_2 and CdS promoting the separation of photogenerated charge carriers in TiO_2 and CdS. Under UV irradiation, the photogenerated electrons migrated from TiO_2 to Au and then to CdS. The photogenerated electrons in the conduction band of CdS are employed for the reduction reaction, while the photogenerated holes in the valance band of TiO_2 are used for the oxidation reaction. A selective deposition of Pt onto CdS further accelerated the H_2 evolution. The transfer of electrons from CdS to TiO_2 has been confirmed to be a minor path. This is quite different from the situation in which CdS is employed as a sensitizer of TiO_2. The Z-scheme mechanism also restricts the photocorrosion of CdS due to the oxidation of surface S^{2-} by the photogenerated holes in the valance band of CdS, because these holes have been recombined with electrons from TiO_2 *via* Au. In some PS–C–PS systems, the conductor has the same metallic element as the artificial PSI or PSII. Under suitable conditions the conductor can be *in situ* generated from the photocatalyst. In general, the *in situ* formed conductor can be stably embedded in the surface of a photocatalyst, which can inhibit exfoliation of the conductor from the photocatalyst surface as compared to the photodeposition method. Furthermore, the tight solid has low electric resistance, which is beneficial for the formation of Ohmic contact. Silver halides (AgX, X = Cl, Br, I) are famous photosensitive materials with significant application in the photography field due to their particular photolysis characteristics. In addition, silver halides have also proved to be excellent photocatalysts for the degradation of organic pollutants and the inactivation of bacteria.[72] Generally, Ag nanoparticles are unavoidably generated in the photocatalytic reaction due to the photo-induced decomposition of AgX. He *et al.*[73] reported a Ag_3PO_3–Ag–g-C_3N_4 catalyst showing a CO_2 conversion rate of 57.5 µmol h^{-1} under simulated sunlight irradiation, which is 6.1 and 10.4 times higher than that of g-C_3N_4 and P25, respectively. As shown in Figure 6.7(A) the photocatalytic system follows a Z-scheme mechanism *via* photo-induced formed Ag as a conductor. Similarly, a visible-light-driven Ag_3PO_4/Ag/SiC photocatalyst follows the Z-scheme mechanism for degradation of pollution.[74] Kim *et al.* prepared the nanocomposite catalyst WO_3–W–$PbBi_2Nb_{1.9}Ti_{0.1}O_9$ by deposition of W clusters onto $PbBi_2Nb_{1.9}Ti_{0.1}O_9$ perovskite followed by partly oxidizing W to WO_3 on the top layers.[75] Under visible-light (λ > 420 nm) irradiation, the photogenerated electrons in the conduction band of WO_3 could not reduce H_2O to H_2 because of the lower position of the conduction band of WO_3. Instead, these electrons migrated to W and recombined with the photogenerated holes from $PbBi_2Nb_{1.9}Ti_{0.1}O_9$. At the same time, the photogenerated electrons in the conduction band of $PbBi_2Nb_{1.9}Ti_{0.1}O_9$ could work for the reduction of H_2O to H_2 and the holes in the valance band of WO_3 functioned for the oxidation of H_2O to O_2. The key point here is the creation of a W layer to separate two semiconductors, yielding an Ohmic contact between them (Figure 6.7B). Without this Ohmic layer, the simple p–n junction structure is less effective. Polymer graphene is also used in engineering Z-scheme photocatalytic systems by acting as an "artificial lawn" for the transfer of electrons, similar to the function of metal conductors in PS–C–PS systems. Li *et al.*[76] designed a Z-scheme consisting of $Fe_2V_4O_{13}$ nanoribbons and CdS nanoparticles as the visible-light active photocatalysts and reduced graphene oxide (RGO) as a solid electron mediator. It exhibits good performance in the conversion of CO_2 into CH_4. RGO as an interlayer between $Fe_2V_4O_{13}$ and CdS offers a high speed charge transfer channel, leading to enhanced charge separation efficiency, and also protects CdS against photocorrosion (Figure 6.7C).

In the PS–PS systems the properties of the solid–solid contact interface between PSII and PSI determine the resistance level of electron transfer, which strongly depends on the formation method of the contact interface. Based on the properties of the solid–solid contact interface, the formation of this interface can be divided into physical and chemical methods. The physical formation utilizes the interparticle electrostatic adsorption to connect PSII and PSI. In the Z-scheme $BiVO_4$–Ru/$SiTiO_3$:Rh system constructed by mixing the powders of $BiVO_4$ and Ru/$SrTiO_3$:Rh the highest photocatalytic activity for water splitting was achieved at pH of 3.5, which is ascribed to opposite charges of PSI and PSII at such a pH value based on their zeta potential.[77,78] Unlike the physical method, the chemical method uses one semiconductor as a substrate and loads another semiconductor onto the surface of the former by chemical reaction. In general, the solid–solid contact interface prepared by the chemical method is more stable than that obtained by the physical one because the former probably connects PSII and PSI by strong

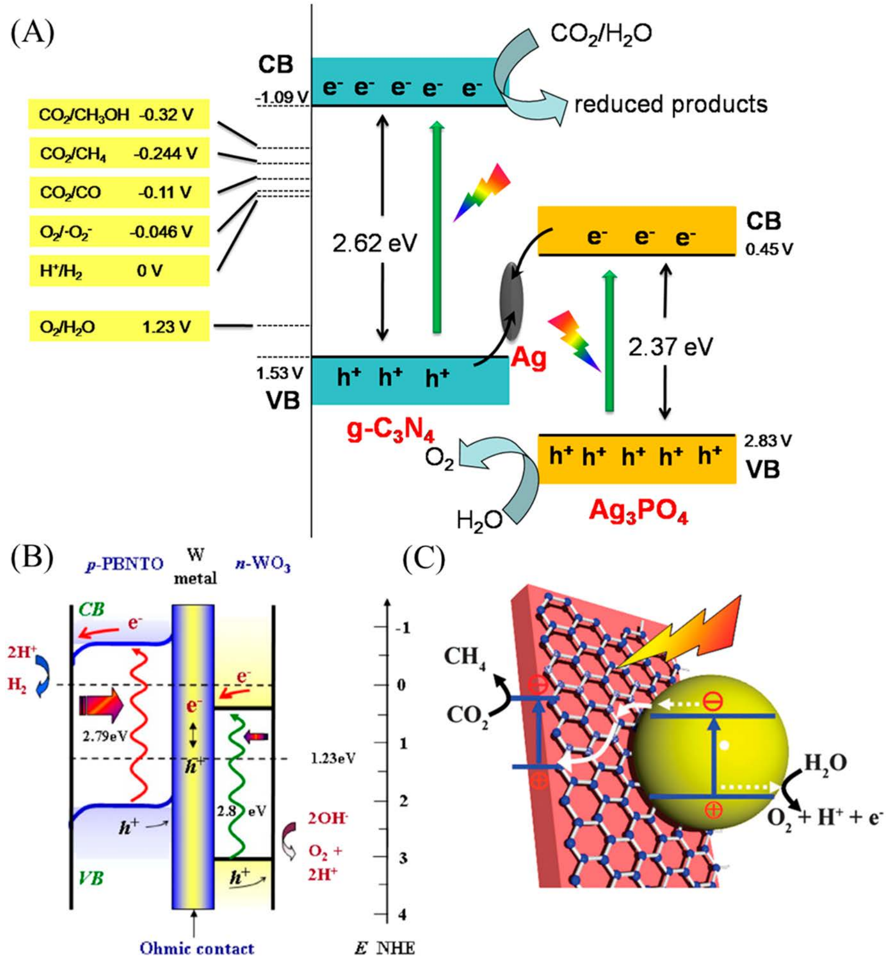

Figure 6.7 Schemes describing the photocatalytic mechanism of (A) Ag_3PO_4/Ag/g-C_3N_4 composites, (B) WO_3–W–$PbBi_2Nb_{1.9}Ti_{0.1}O_9$, and (C) $Fe_2V_4O_{13}$/RGO/CdS. ((A) Reprinted with permission from ref. 74. Copyright 2015 American Chemical Society. (B) Reprinted with permission from ref. 75. Copyright 2006 American Institute of Physics. (C) Reproduced from ref. 76 with permission from The Royal Society of Chemistry.)

chemical bonds. A recent study claimed that the pencil-like one-dimensional CdS–ZnO composite prepared by a solvothermal reaction followed by *in situ* growing method could follow the Z-scheme mechanism, resulting in high H_2 evolution rates.[79] The highest H_2 production rate of 1.805 mmol g^{-1} was achieved with a $(CdS)_{0.2}$–$(ZnO)_1$ catalyst. Similarly, CuO–TiO_2 composite calcined at 450 °C and CTAB as a dispersant was evaluated for photocatalytic reduction of CO_2 in the presence of methanol as a sacrificial reagent under UV-light illumination.[80] The photocatalytic reduction of CO_2 formed methyl formate and the reaction proceeded *via* a Z-scheme. It was proposed that the photogenerated electrons in the conduction band of CuO were used for the reduction of CO_2, and the photogenerated holes in the valance band of TiO_2 were consumed by the sacrificial reagent methanol. The interface between CuO and TiO_2 favored the combination of holes from CuO and electrons from TiO_2, playing an important role in enhancing the photocatalytic activity. The rate of methyl formate production was ~1600 μmol g^{-1} h^{-1} over 1.0 wt% CuO–TiO_2. In addition, $WO_3/CdWO_4$,[81] $BiVO_4$/g-C_3N_4,[58] TiO–g-C_3N_4,[82] and Ag_3PO_4/g-C_3N_4[57] also follow the Z-scheme mechanism in the degradation of organic pollutant, hydrogen production, decomposition of formaldehyde, and CO_2 reduction, respectively.

The verification of Z-scheme electron transfer in water splitting needs to satisfy three conditions: (1) PSII can only produce O_2 in the presence of electron acceptor, (2) PSI can only produce H_2 in the presence of electron donor, and (3) steady overall water splitting can occur in the simultaneous presence of PSII and PSI and in the absence of electron acceptor and donor. Similarly, the Z-scheme electron transfer in CO_2 reduction reaction can also be verified by detecting the oxidation (O_2) and reduction ($C_xH_yO_z$) products. For the degradation of pollutants, the detection of active oxidant species is an indirect method to verify the Z-scheme electron transfer in the photocatalytic degradation. In general, the roles of hydroxyl radical ($^{\bullet}OH$), superoxide anion ($^{\bullet}O_2^-$), and photogenerated hole (h^+) in the photocatalytic degradation are determined by comparing the performance of photocatalysts before and after adding their corresponding scavengers. If active oxidant species play a dominant role in the photocatalytic degradation, the addition of its corresponding scavenger will lead to a sharp decrease in the photocatalytic performance. In contrast, the addition of a scavenger will have little effect on the performance of a photocatalytic system if its corresponding active oxidant species plays a negligible role in the photocatalytic degradation. An enhanced visible-light-driven MoO_3/g-C_3N_4 photocatalyst was prepared by a simple mixing–calcination method.[83] The working mechanism of MoO_3/g-C_3N_4 catalyst was determined by potential comparison and active species trapping O_2^- and h^+ were verified to be the reactive species during the photocatalytic oxidation of MO by adding benzoquinone (BQ, O_2^- scavenger), KI (KI, $^{\bullet}OH$ and h^+ scavenger), and isopropanol (IPA, $^{\bullet}OH$ quencher) as scavengers. Since the conduction band potential of MoO_3 is lower than the standard reduction potential of $^{\bullet}O_2^-/O_2$, the MoO_3/g-C_3N_4 can be speculated to follow a Z-scheme mechanism (as shown in Figure 6.8b) rather than a charge transfer mechanism (Figure 6.8a). In addition, the isopropanol scavenger displayed a stronger effect on the photo-activity of MoO_3–g-C_3N_4 than on that of g-C_3N_4. This phenomenon suggests an increase in $^{\bullet}OH$ concentration in the MoO_3–g-C_3N_4 composite, which is in a good agreement with the expectation of the Z-scheme mechanism. Ye *et al.*[84] used a similar method to investigate the degradation mechanisms of AgX/Ag/BiOX (X = Cl, Br) for RhB photodegradation and proposed metallic Ag inducing surface plasmon resonance (SPR) as well as the presence of a Z-scheme bridge for AgCl/Ag/BiOCl and AgBr/Ag/BiOBr.

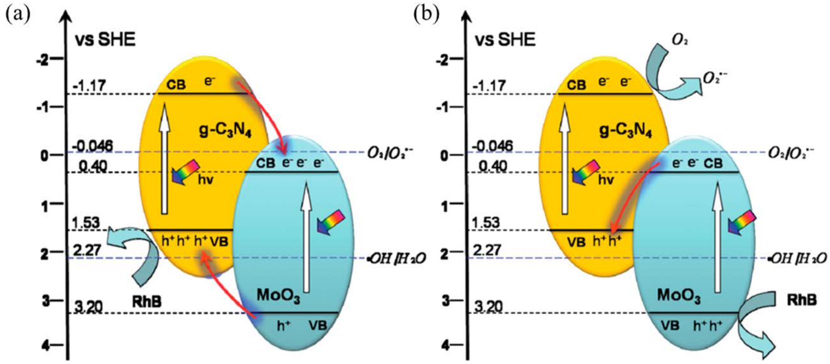

Figure 6.8 Possible schemes for electron–hole separation and transport at the visible-light-driven MO_3–g-C_3N_4 composite interface: (a) charge transfer mechanism; (b) Z-scheme mechanism. (Reproduced from ref. 83 with permission from The Royal Society of Chemistry.)

It is well known that a large number of defects can be easily aggregated at the solid–solid contact interface. Thus, the energy levels of the solid–solid contact interface are quasi-continuous, which is similar to the situation with conductors, implying that the solid–solid contact interface shows similar properties to conductors at a certain level, such as low electric resistance. Therefore, like the conductor in a PS–C–PS system, the solid–solid contact interface can also form an Ohmic contact. Generally, the conductor in the PS–C–PS systems shows stronger ability for charge transfer than solid–solid contact interfaces in the PS–PS systems due to the difference in their electrical resistances, which can be tuned by optimizing the formation and treatment of the solid-state photocatalytic systems. Compared with liquid phase PS–A/D–PS systems, solid-state photocatalytic systems have a larger potential in practical applications and will probably attract more attention in future.

Similar to the heterojunction-type photocatalytic system, the artificial Z-scheme photocatalytic system is also characterized by the spatial isolation of photogenerated electrons and holes, which benefits the separation of photogenerated electrons and holes. Moreover, the aggregation of photogenerated electrons in the CB of PSI and holes in the VB of PSII makes PSI and PSII an electron-rich and hole-rich region, respectively, which can suppress the photo-oxidation of PSI and the photoreduction of PSII. However, the number of photogenerated electrons and holes in the Z-scheme photocatalytic system is smaller than that in the normal heterojunction-type photocatalytic system under same conditions because of the electron–hole recombination in the Z-scheme system. Nonetheless, the Z-scheme photocatalytic systems still receive a lot of attention due to their potential for solving the energy and environmental crises *via* this unique electron transfer way. However, the Z-scheme photocatalytic systems are still at an initial stage, although numerous attempts have been made so far. The stability, light harvesting, redox ability, charge separation, and transfer of the existing

Z-scheme photocatalytic systems are far from fulfilling the requirements of practical significance, and need to be further investigated.

6.5 Plasmonic Photocatalysis

Plasmonic photocatalysis has recently come into focus as a very promising technology for high-performance photocatalysis. The term "plasmonic photocatalysis" was created by Awazu *et al.* in 2008.[85] The "plasmonic" in this term refers mainly to the localized surface plasmon resonance (SPR) and the induced effects. SPR can be described as the resonant photo-induced collective oscillation of valence electrons, established when the frequency of photons matches the natural frequency of surface electrons oscillating against the restoring force of positive nuclei. The resonant photon wavelength varies for different metals. The resonant wavelength and SPR intensity depend not only on the nature of the metal, but also on the size and shape of metallic nanostructures. The absorption wavelength in the visible range is the source of energy for photocatalysis. The noble metal nanoparticles may enhance the optical absorption in two ways: surface plasmon absorption by the metal nanoparticles and photon path length increase in the semiconductor surface region. The resonant wavelength and local electric field are affected by the local environment and nanoparticle size and/or shape (Figure 6.9).[86,87] By manipulating the composition, shape, and size of plasmonic nanoparticles, it is possible to design nanostructures that interact with the entire solar spectrum and beyond. The absorption wavelength is redshifted if the surrounding medium has a higher dielectric constant (redshift of ~100 nm if refractive index is increased by 1) or the nanoparticle size increases. The large metal nanoparticles scatter the unabsorbed photons efficiently, increasing the average photon path length, and produce more absorption near the semiconductor surface. Hu *et al.*[88] compared the absorption spectra of Ag/AgBr/TiO_2 composite, pure TiO_2, and Ag/TiO_2 and found that Ag/TiO_2 has much larger absorption in the visible range (>400 nm) than TiO_2, which is attributed to the SPR. A broadening of the absorption peak is mainly due to the non-uniformity of the Ag nanoparticle size. The Ag/AgBr/TiO_2 composite also exhibits an obvious absorption of visible light, which should result from the indirect bandgap transition of AgBr and the SPR of Ag, with the former being the dominant effect. Christopher *et al.*[89] studied the influence of the shape of Ag nanoparticles in the Ag@TiO_2 composite on the enhancement of the photoreaction rate. It was found that Ag nanocubes (edge length 79 nm) had the highest photoreaction rate when compared to Ag nanospheres (diameter 75 nm) and Ag nanowires (diameter 90 nm, aspect ratio > 30). Such a difference was attributed to the scattering efficiency of the nanostructure and a simulation showed that the Ag nanocubes had the highest scattering efficiency. In addition to the size and shape, the enhancement by scattering is also strongly dependent on the loading level of the metal nanoparticles. In plasmonic photocatalysis the noble metal nanoparticles could form different contacts with the photocatalyst. As shown in Figure 6.9(c), when a silver

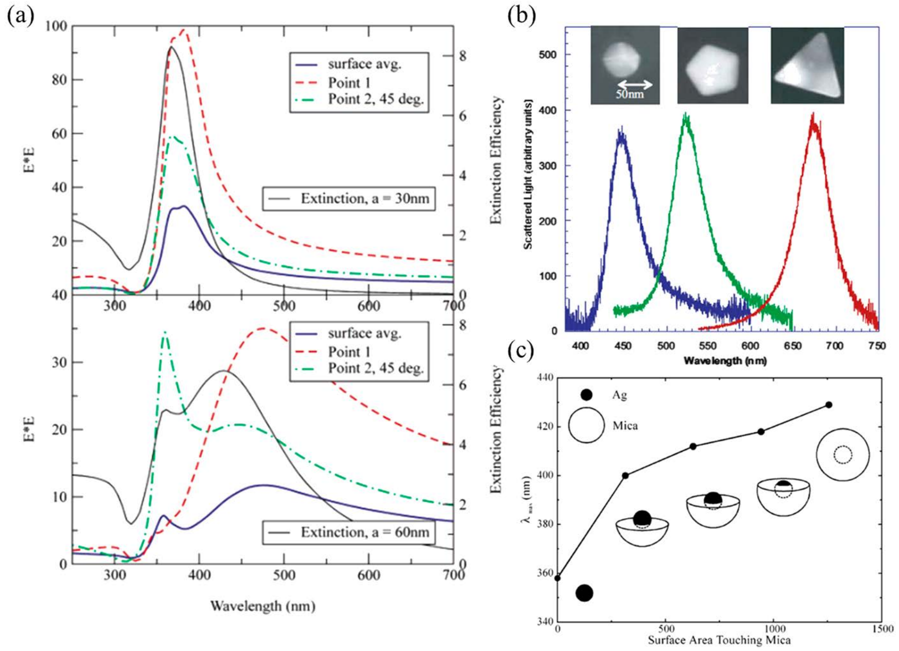

Figure 6.9 Effect of (a) size, (b) shape, and (c) local environment of the noble metal nanoparticles on their absorption properties. ((a), (c) Reprinted with permission from ref. 86. Copyright 2003 American Chemical Society. (b) Reprinted with permission from ref. 87. Copyright 2002 American Institute of Physics.)

nanosphere (~10 nm) is gradually embedded into a mica shell (10 nm thick) the resonant wavelength is redshifted from 350 to 430 nm with increasing contact area, which is thus beneficial to plasmonic photocatalysis.[86]

Plasmonic photocatalysis involves dispersal of noble metal nanoparticles (mostly Au and Ag, in sizes of tens to hundreds of nanometers) into semiconductor photocatalysts to obtain a drastic enhancement of photo-activity under the irradiation of UV and a broad range of visible light. Compared with common semiconductor photocatalysis, plasmonic photocatalysis possesses two distinct features, a Schottky junction and localized surface plasmon resonance. The synergy of noble metal and semiconductor photocatalyst brings in significant changes to many aspects of the photocatalysis, including enhanced optical absorption, local electric field, and the excitation of active electrons and holes and separation of charge carriers. In addition, the surface plasmons polarize the reactant molecules in the fluid and enhance adsorption to the metal surface. The surface plasmons also heat up the local environment, increasing the mass transfer of the molecules and enhancing the reaction rates. Moreover, the metal acts as a "fast lane" for the excited electrons (or holes) to transfer to the metal/fluid interface, trapping them on the metal surface and increasing the contact area (and thus the reaction rate) with the targeted reactants. Generally speaking, heterogeneous photocatalysis can be broken down into five independent steps: (1) transfer of the reactants onto the photoreaction surface, (2) adsorption of the reactants, (3) redox reactions in the adsorbed phase, (4) desorption of the product from the surface, and (5) transfer of the products away from the surface. Plasmonic photocatalysis contributes to all five steps.[90]

Based on the SPR of noble metals and its effect on the plasmonic photocatalytic system, two main mechanisms have been discussed in the literature regarding plasmonic enhancement of photocatalysis under visible illumination: charge transfer and local electric field enhancement. An immediate effect of SPR is an enhancement of local electric field, which in turn would promote the generation of electrons and holes by a roughly linear relationship. Analysis of gas-phase partial oxidation reactions on excited plasmonic Ag nanostructures established that, at a constant temperature, the reaction rates exhibited strong dependence on the light wavelength, peaking at wavelengths where the plasmon intensity was the highest.[91] These measurements provided a clear indication that the excitation of surface plasmons was responsible for the observed photocatalytic activity. Thomann *et al.*[92] measured the photocurrent enhancement spectrum of Au/Fe_2O_3 photocatalyzed water splitting, finding a peak enhancement of approximately 11-times (Figure 6.10A). They also found that the peak position and the line shape of the photocurrent enhancement depend critically on the position of the nanoparticles in the iron oxide film. The particles on top of the absorber film produce an asymmetric line shape of the photocurrent enhancement, while particles embedded in the film produce a more symmetric spectral feature. Electromagnetic simulations using the finite-difference time-domain method have shown that the electric field intensity of local plasmonic "hot spots" can reach as much as 1000 times that of the incident electromagnetic field.[93] Mizeikis *et al.*[94] performed simulations of optical field enhancement on a system consisting of spherical and hemispherical noble metal nanoparticles on a smooth titania surface using the same method. Large near-field enhancement factors up to 104 were obtained at the metal/titania interface in their simulation. Hou *et al.*[95] have attributed photocatalytic enhancement to this plasmonic local electric field enhancement. Several other groups have also adopted the local electric field enhancement mechanism. Lu *et al.*[96] ascribed a 2.3-fold increase in 2,4-dichlorophenol degradation by Au nanoparticle/TiO_2 to the enhanced light harvesting caused by the surface plasmon resonance. Duan *et al.*[97] investigated enhanced electron–hole pair generation rates in CdS by the enhanced near-field amplitudes of the surface plasmon resonance on the Ag surface in a Ag/SiO_2/CdS multilayer nanocomposite.

However, the role of SPR has two sides. Lin *et al.*[98] investigated Au/TiO_2 and demonstrated experimentally that both pros and cons of SPR exist simultaneously in the photocatalytic reaction, as shown schematically in Figure 6.10(C). When operating under mixed UV and green light irradiation, the SPR injected hot electrons (from Au nanoparticles to TiO_2 under green light

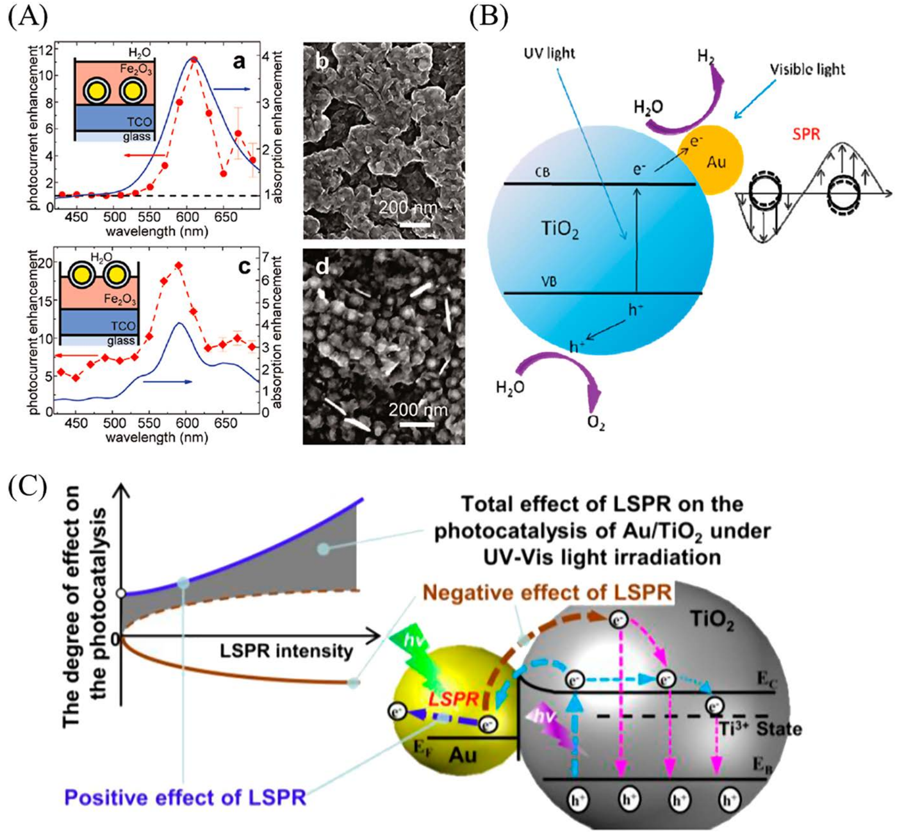

Figure 6.10 (A) Photocurrent enhancement spectra comparison for Au nanoparticles with a silica shell embedded in and on top of 100 nm thin Fe_2O_3; (B) The schematic mechanism of Au/TiO$_2$ SPR photocatalytic systems; (C) The pros and cons of surface plasmon resonance Au/TiO$_2$ photocatalysis systems. ((A) Reprinted with permission from ref. 92. Copyright 2011 American Chemical Society. (B) Reprinted with permission from ref. 99. Copyright 2011 American Chemical Society. (C) Reproduced from ref. 98 with permission from The Royal Society of Chemistry.)

irradiation) may surmount the Schottky barrier formed between Au nanoparticles and TiO$_2$, and flow back into the TiO$_2$. As a result, these electrons may compensate and even surpass those transferred from TiO$_2$ to Au nanoparticles, thus accelerating the recombination of UV excited electron–hole pairs in TiO$_2$. On the other hand, more hot electrons existing on the Au nanoparticles surface due to the SPR would favor the photocatalytic reaction, which, accompanied by the negative effect, dominates the overall photocatalytic performance.

Apart from the enhanced optical absorption and local electric field, a plasmonic photocatalysis can also enhance the separation of charge carriers. In this case, the noble metal and the semiconductor form a space-charge region (*i.e.* Schottky junction) when the noble metal nanoparticles have direct contact with the semiconductor. This considerably enhances the separation of photo-excited electrons and holes, drastically reduces the chance of recombination, and significantly increases the lifetime of the photo-excited charge carriers.[100,101] This effect has been considered as one of the major contributors to enhanced photocatalytic efficiency, which is influenced by many factors, such as the type of semiconductor, the irradiation state, and the relative position of the semiconductor's Fermi level to the work function of the metal. Plasmonic photocatalysis presents an enhanced utilization of light by the suppression of electron–hole recombination and the efficient conversion of light energy into localized heat. During the reaction process, charge carriers are directly injected from excited plasmonic metal nanostructures into the semiconductor surface. The charge injection mechanism is analogous to dye sensitization, where a dye molecule, anchored to a semiconductor, acts to absorb light and transfer energetic charge carriers to the semiconductor. In 2004, Tian *et al.*[102] proposed a charge transfer mechanism to explain their experimentally observed photo-to-current conversion efficiency enhancement under visible light illumination upon loading Au or Ag nanoparticles into TiO_2 sol–gel films. In their proposed charge transfer mechanism the plasmon resonance excites electrons in Au or Ag, which are then transferred to the conduction band of the adjacent TiO_2. Furube *et al.*[103] and Moskovits *et al.*[104] successively explained this charge transfer mechanism, in which the surface plasmon decay produces electron–hole pairs in the gold. The resulting hot electrons are then directly injected into TiO_2 by quantum tunneling. Similar results were obtained by Jiang *et al.*[105] However, notably, these carrier dynamics studies did not involve redox reactions, and therefore were not limited by the Fermi energy of the metal, which lies below the potential of the reduction half reaction. Dong *et al.*[106] explored AgCl–$SmVO_4$ and AgI–$SmVO_4$ catalysts. The photo-excited electrons in the *in situ* reduced Ag nanoparticles or the AgX particles can be further transferred to $SmVO_4$, yielding a better separation of the electrons and holes. In addition, nanostructure $SmVO_4$ can enhance the specific surface area. For this reason, Ag/AgX/$SmVO_4$ is expected to have a better (at least comparable) performance in photocatalysis than Ag/AgX. Dinesh *et al.*[107] have reported that metal nanoparticles can also act as a reservoir for photogenerated electrons in semiconductors *via* the investigation of hybrid ZnO@Ag core–shell heterojunction nanorods synthesized using hydrothermal and seed mediated growth techniques. The enhanced photocatalytic property observed for ZnO@Ag hybrid core–shell nanorods is attributed to a phenomenal increase in oxygen related defects in the core that generate photo-induced charge carriers and the presence of plasmonic Ag nanoclusters in the shell, which act as a sink for the photo-induced charge carriers. This storage of electrons in metal nanoparticles reduces charge recombination, thereby enhancing the photocatalytic activity. For a few plasmonic photocatalysts, the metal nanoparticles play multiple roles simultaneously. Chen *et al.*[99] prepared Au/TiO_2 by the photodeposition method and investigated its photocatalytic performance in water splitting. As shown in

Figure 6.10(B), the loaded Au nanoparticles not only act as electron traps and active sites but also play an important role in the SPR electric field enhancement. An enhanced performance of Au/Bi_2WO_6 for both selective alcohol oxidation and Cr(VI) reduction can also be attributed to the increase in the formation rate of electron–hole pairs of Bi_2WO_6 induced by SPR of Au NPs and higher efficiency of electron transfer due to the energy barrier between the conduction band of Bi_2WO_6 and the Fermi energy of Au NPs.[108]

Several research targets have been pursued to render TiO_2 responsive to visible light, or enhance the photocatalytic efficiency of visible light-responsive photocatalysts, and study the enhancement mechanisms and the influences of nanoparticle properties, and expand the applications of plamonic photocatalysis to water splitting, CO_2 reduction, bacteria destruction, and more. Although the metal nanoparticles could contribute to the photocatalytic efficiency through the different mechanisms, some adverse effects have also been spotted. First, the metal nanoparticles on the surface of the semiconductor have a shading effect by reducing the light-receiving area of the semiconductor. They also take up some surface area of the semiconductor and may even block the pores of the semiconductor. In addition, the inclusion of noble metals limits the process temperature to hundreds of degrees, while high-temperature annealing of the mixture is often needed to increase the crystallization and thus enhance the photo-activity of the semiconductor. Moreover, the metal nanoparticles could act as a recombination center and might undergo photocorrosion and leaching, causing a gradual loss of the photocatalytic performance.

Although still in its infancy, plasmonic photocatalysis has already demonstrated its amazing capability to tackle two fundamental problems of current photocatalysis – low photocatalytic efficiency and low response to sunlight. Significant enhancement of photocatalytic efficiency, typically up to ten times larger, has been routinely obtained. Materials strongly responsive to visible-light have now been made available by tailoring the size and shape of noble metal particles and by specific design of the material structure and composition. There is still plenty of room for further physical, material, and applied studies of plasmonic photocatalysis. Study of the physical mechanisms of plasmonic photocatalysis requires more effort, as it is really quite complicated and the reported studies are quite scattered. A unified, widely accepted, all-in-one theoretical scheme remains to be found. In addition, new plasmonic photocatalyst materials with better performance and lower cost are still at the top of the "wanted" list. In the long run, the material cost will be a limiting factor even if the noble metal-based plasmonic photocatalysts achieve high efficiency and stability under sunlight irradiation. Noble metals are expensive and rare, and photocorrosion could cause a gradual release of the noble metal nanoparticles into solution, which is undesirable in water purification. Other metals that are relatively cheap and abundant such as Al and Cu, as well as other attractive carbon-based nanomaterials such as RGO, GO, and carbon quantum dots, may be explored. Moreover, new reactors designed specifically for plasmonic photocatalysis may need more attention, and it should be valuable to extend the wavelength response region to the near-infrared using plasmonic photocatalysis.

6.6 New Applications of Photocatalysis

Growing endeavors have been devoted to applying photocatalysis, a green technique, to photocatalytic selective transformations. Although photocatalytic processes generally have been thought to be highly unselective, recent progress indicates that semiconductor photocatalysis can also serve as an alternative to conventional synthetic routes for synthesis of fine chemical or biomass-derived carbohydrate through the selection of appropriate photocatalysts and control of the reaction conditions. It is now recognized that heterogeneous photocatalysis holds great potential for organic synthesis due to its possibility to avoid environmentally unfriendly heavy metal catalysts, strong chemical oxidants or reducing agents, such as Cr(IV), MnO_4^-, ClO^-, Cl_2, H_2, and CO, as well as harsh reaction conditions such as high temperature and high pressure.

Biomass, especially that which exists in the form of inedible lignocellulosic materials such as grasses, woods, and crop residues, serves as renewable feedstock and could be considered as an alternative source of the chemicals and energy currently derived from petroleum. Green conversion and application of biomass is desirable from economic and environmental perspectives.

Cellulose, as the largest part of lignocellulose and the most abundant biopolymer on earth, consists of D-glucose linked by β-1,4 bonds. Studies on conversion of cellulose into biofuels and other biomaterials is currently a worldwide activity. In most literature reports, cellulose, as an agriculture waste, was decomposed by a photocatalysis process to CO_2. Recently, cellulose has been used effectively in other ways, by acting as sacrificial biomass for photocatalytic H_2 evolution from water, as a biotemplate for synthesis of photocatalyst, and as biomass feedstock for photosynthesis of biomass-derived platform chemicals. In the last case, there are few literature reports due to the fact that cellulose is insoluble, crystalline microfibril, and difficult to react with other compounds. For degradation of cellulose to 5-hydroxymethylfurfural (5-HMF), a cylindrical photocatalytic corrugated plate reactor coated with anatase TiO_2 thin film (Figure 6.11A) was developed.[109] The concentrated $ZnCl_2$ solution used not only dissolves the cellulose as a solvent but also, as a Lewis acid, helps to break down the glycosidic linkage for the hydrolysis of monosaccharide from cellulose degradation. The product 5-HMF is obtained with a yield of 3.87 g L^{-1} after 2 h UV irradiation (21 W), over nine cycles coated TiO_2 photocatalyst with a corrugated plate angle of 42°. It opens a window for photo-conversion of cellulose to biomass-derivate platform chemical. However, the yield is far from the level obtained *via* chemical conversion, and thus more effort should be made for the photocatalysis of cellulose.

Chitin is the second most abundant naturally occurring biopolymer and is found in various biosystems, including fungal cell walls, the exoskeleton of crustaceans, skeletal tissue of mollusks, and the integument

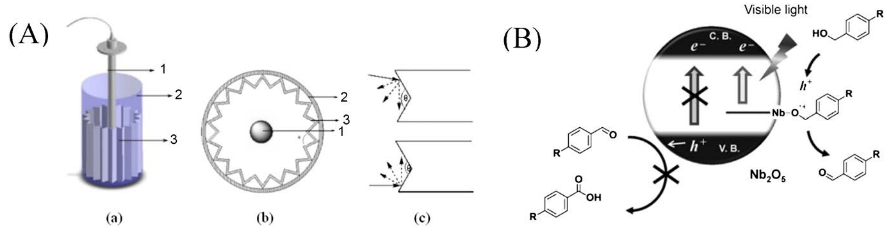

Figure 6.11 (A) Experimental setup of the corrugated plate reactor: (a) overall view; (b) top view; (c) corrugated plate reactor angle (θ) and UV light diffuse emission on the plate. (1): UV light; (2): reactor tube; (3): corrugated plate coated with TiO_2; (B) scheme of alcohol photocatalytic oxidation over Nb_2O_5. ((A) Reprinted with permission from ref. 109. Copyright 2011 John Wiley & Sons. (B) Reprinted with permission from ref. 120. Copyright 2014 John Wiley & Sons.)

of insects. Chitosan, the deacetylated derivative of chitin, is one of the nontoxic and biodegradable carbohydrate polymers, and has received much attention as a functional biopolymer for diverse applications from pharmaceuticals to commodity chemicals. These functions undoubtedly depend upon not only their chemical structure but also the molecular weight, which is closely related with its solubility and application. Therefore, it is necessary to produce different molecular weights of chitosan. TiO_2 photocatalyst was also applied for the degradation of chitosan.[110] In a mild photocatalytic process the photocatalytic oxidation of chitosan took place without altering much of the overall polymeric structure of chitosan. However, the primary alcoholic group ($-CH_2OH$) was lost – accompanied by the formation of the carbonyl (C=O) side groups and partial elimination of amino groups.

Selective oxidation is an important method for bringing functionality into both petroleum- and biomass-based feedstock because it is often the first step to high-value fine chemicals, agrochemicals, and pharmaceuticals. The oxidation of alcohols to aldehydes is one of those elementary reactions that are of fundamental importance in both the laboratory and commercial procedures. The process is often carried out using corrosive and stoichiometric oxygen donors such as chromate or permanganate and generally transition-metal catalysts. In recent years, heterogeneous photocatalysis has been developed in alcohol oxidation reactions at the expense of solar energy.

Titanium dioxide (TiO_2) is one of the most important and widely applied photocatalysts for oxidation of alcohol owing to its high photo-activity, low cost, low toxicity, and good chemical and thermal stability. Pure TiO_2 photocatalyst can be used in selective oxidation of the biomass-derivate chemical 5-HMF, which is considered to be a versatile platform compound and a crucial intermediate for connecting biomass resource and the fossil industry because that it can be further transformed into a series of high-quality fuels such as 2,5-dimethylfuran (DMF), C_9–C_{15} alkanes, and high-value chemicals such as 2,5-diformylfuran (DFF). TiO_2 samples with different crystalline phase and crystallinity were compared, and a DFF selectivity of 22% could be obtained even on poorly crystalline TiO_2 catalyst.[110,111] Although the selectivity is far lower than that obtained *via* a conversional chemical oxidation, it opens up routes for important improvements, *i.e.* increase of crystallinity and replacement of the UV light absorber TiO_2 by a visible light responsive photocatalyst. Noble metal (Pt, Au, Rh *etc.*), oxides/sulfides, hybrid polyoxometalates, and organosilicons have been used to modify TiO_2 with different morphologies for photo-oxidation of alcohols.[112–116] Apart from TiO_2 many other, visible light responsive catalysts have been developed for the photocatalytic oxidation of alcohols.[117–119] Although the band gap of Nb_2O_5 is 3.4 eV, Nb_2O_5 can effectively photo-oxidize alcohol to the corresponding aldehydes under visible light (>400 nm) irradiation with high selectivity; this is attributed to the special mechanism, which differs from that on TiO_2, as shown in Figure 6.11(B). First, alcohol is adsorbed onto Nb_2O_5 to form an alcoholate, which is activated by transferring an electron to the conduction band, reducing Nb^{5+} to Nb^{4+} while leaving a hole on the alcoholate. Then, the formed alkenyl radical is converted into a carbonyl compound. Finally, the product is desorbed and then the reduced Nb^{4+} sites are reoxidized by reaction with molecular oxygen.[120]

Graphene and g-C_3N_4 can also be used in organic photosynthesis. As mentioned above, g-C_3N_4 has an appropriate band gap and also band positions. These properties allow it to be visible-light photosensitive, by which the photoinduced electron can activate oxygen and reduce O_2 to active $^{\bullet}O_2^-$. Therefore, it can be envisioned that g-C_3N_4 would act as a desirable visible light responsive photocatalyst for the oxidation of alkanes, olefins, alcohols, *etc.* It was recently found that g-C_3N_4 is indeed an active metal-free photocatalyst with high selectivity for direct oxidation of benzene to phenol under mild conditions.[121] Using hydrogen peroxide as a clean oxidant, at a reaction temperature of 670 °C and under the irradiation of visible light (>420 nm), fluorine-doped carbon nitrides showed improved activities compared to bare g-C_3N_4 in the catalytic oxidation of benzene to phenol. The combination of g-C_3N_4 with Fe can increase the photocatalytic activity. After Fe–g-C_3N_4 is deposited into SBA-15 or titanium silicate zeolite (TS-1), the catalytic activity could be further improved. Su *et al.*[122] found that mesoporous g-C_3N_4 can activate molecular oxygen for the oxidation of benzyl alcohol to benzaldehyde with high selectivity (>99%). Both the electron-withdrawing and electron-donating substituent of the aromatic ring can enhance the rate of the reaction. Zhang *et al.*[11] prepared graphene–TiO_2 composites by interfacial tailoring the unique 2D material graphene with TiF_4 as precursor *via* a facile two-step wet-chemistry approach and applied them for selective oxidation of alcohols to aldehydes with oxygen as oxidant under mild conditions. Compared with its analogue carbon nanotube (CNT)–TiO_2 featuring a poor interfacial contact, the graphene–TiO_2 nanocomposites with an intimate interfacial contact exhibited much enhanced visible light photoactivity. The superior structure-directing role of GO over CNT is beneficial to a more intimate interfacial contact between GR and TiO_2, thus leading to better separation of the photogenerated carriers over graphene–TiO_2. Therein, 5% GR–TiO_2 can photocatalyze a range of benzylic alcohols and allylic alcohols to the corresponding aldehydes under visible light irradiation with high selectivity (90–100%). The photo-activity of graphene–TiO_2 can be further enhanced by decreasing the defects of graphene and increasing interfacial contact between graphene and semiconductor TiO_2. CdS–GR synthesis by a one-step solvothermal approach can also exhibit enhanced photo-activity towards selective oxidation of alcohols to their corresponding aldehydes, which is attributed to the integrative effect of the enhanced light absorption intensity, high electron conductivity of GR, and its significant influence on the morphology and structure of the catalyst.[123]

The present environment and energy situations urge us to modify the independence from fossil fuel and conventional chemical processes. This can be achieved by the development and employment of new technologies that exploit the inexpensive and renewable resource biomass, especially inedible biomass. The photocatalysis of biomass or biomass-derivate chemicals fits into the trend to "green sustainable development", since it opens a new window for exploration of new processes. Over the past few years, considerable interest has emerged in the application of photocatalysis in the field of biomass conversion. Among several unresolved problems, the low selectivity of the target production and inadequate new products based on biomolecules are the most troublesome. Nevertheless, a relatively small number of data already proves that engineered goal-directed photocatalysts create a promising alternative in this field and open up a broad variety of new opportunities.

6.7 Perspectives

Although great progress have been achieved in photocatalysis in recent years, more efforts should focus on a few areas: the development of robust predictive models, new synthetic strategies that would allow for the design of targeted composite photocatalysts, new reactor designs, new technology for old reactions, new applications such as biomass photocatalysis, and a deep understanding of mechanisms. The finding of novel applications should be based on a better comprehension of the physicochemical properties of photocatalysts, which will undoubtedly lead to more exciting results.

Opportunities as well as challenges exist together for the development of novel multifunctional photocatalytic systems. With the reasonable design and full exploration of their photocatalytic potential, the applications of bi- or multi-component hybrid photocatalysts for the conversion of solar to chemical energy could significantly be enriched in a more rational way. Intense and rational efforts carried out recently between academia and industry would open up new routes to form clean and renewable energy by utilizing novel photocatalytic materials in new reactions.

References

1. K. S. Novoselov, A. K. Geim, S. V. Morozov, D. Jiang, Y. Zhang, S. V. Dubonos, I. V. Grigorieva and A. A. Firsov, *Science*, 2004, **306**, 666.
2. A. K. Geim and K. S. Novoselv, *Nat. Mater.*, 2007, **6**, 183.
3. A. K. Geim, *Science*, 2009, **324**, 1530.
4. D. R. Dreyer, R. S. Ruoff and C. W. Bielawski, *Angew. Chem., Int. Ed.*, 2010, **4**, 99336.
5. K. S. Kim, Y. Zhao, H. Jang, S. Y. Lee, J. M. Kim, K. S. Kim, J. H. Ahn, P. Kim, J. Y. Choi and B. H. Hong, *Nature*, 2009, **457**, 706.
6. X. S. Li, W. W. Cai, J. H. An, S. Kim, J. Nah, D. X. Yang, R. Piner, A. Velamakanni, I. Jung, E. Tutuc, S. K. Banerjee, L. Colombo and R. S. Ruoff, *Science*, 2009, **324**, 1312.
7. Z. Y. Juang, C. Y. Wu, A. Y. Lu, C. Y. Su, K. C. Leou, F. R. Chen and C. H. Tsai, *Carbon*, 2010, **48**, 3169.
8. H. Bai, C. Li and G. Q. Shi, *Adv. Mater.*, 2011, **23**, 1089.
9. W. S. Hummers and R. E. Offerman, *J. Am. Chem. Soc.*, 1958, **80**, 1339.
10. H. Zhang, X. Lv, Y. Li, Y. Wang and J. Li, *ACS Nano*, 2010, **4**, 380.
11. N. Zhang, Y. H. Zhang and Y. J. Xu, *Nanoscale*, 2012, **4**, 5792.
12. L. Z. Dong, Y. M. He, H. J. Lin, W. D. Hu, S. S. Wang, M. F. Luo and L. H. Zhao, *Mater. Lett.*, 2014, **122**, 17.
13. W. Gao, M. Wang, C. Ran and L. Li, *Chem. Commun.*, 2015, **51**, 1709.
14. S. Wu, P. Wang, Y. Cai, D. Liang, T. Ye, Z. Tian, J. Liu and C. Liang, *RSC Adv.*, 2015, **5**, 9069.
15. L. Chen, L. Xie, M. Wang and X. Ge, *J. Mater. Chem. A*, 2015, **3**, 2991.
16. H. Lv, Y. Liu, J. Hu, Z. Li and Y. Lu, *RSC Adv.*, 2014, **4**, 63238.
17. H. Huang, K. Liu, Y. Zhang, K. Chen, T. Zhang and N. Tian, *RSC Adv.*, 2014, **4**, 49386.
18. G. Dai, S. Liu, Y. Liang and K. Liu, *RSC Adv.*, 2014, **4**, 34226.
19. X. Lv, J. Shen, J. Wang, Z. Cui and J. Xie, *RSC Adv.*, 2015, **5**, 15993.
20. T. F. Yeh, F. F. Chan, C. T. Hsieh and H. S. Teng, *J. Phys. Chem. C*, 2011, **115**, 22587.
21. X. Y. Zhang, H. P. Li, X. L. Cui and Y. H. Lin, *J. Mater. Chem.*, 2010, **20**, 2801.
22. W. Q. Fan, Q. H. Lai, Q. H. Zhang and Y. Wang, *J. Phys. Chem. C*, 2011, **115**, 10694.
23. A. Iwase, Y. H. Ng, Y. Ishiguro, A. Kudo and R. Amal, *J. Am. Chem. Soc.*, 2011, **133**, 11054.
24. O. Akhavan and E. Ghaderi, *J. Phys. Chem. C*, 2009, **113**, 20214.
25. O. Akhavan, M. Choobtashani and E. Ghaderi, *J. Phys. Chem. C*, 2012, **116**, 9653.
26. P. Kumar, A. Bansiwal, N. Labhsetwar and S. L. Jain, *Green Chem.*, 2015, **17**, 1605.
27. H. Woo, J. W. Kim, M. Kim, S. Park and K. H. Park, *RSC Adv.*, 2015, **5**, 7554.
28. S. Zhuo, M. Shao and S. T. Lee, *ACS Nano*, 2012, **6**, 1059.

29. J. V. Liebig, *Ann. Pharm.*, 1834, **10**, 10.
30. Y. Gong, M. Li, H. Li and Y. Wang, *Green Chem.*, 2015, **17**, 715.
31. Y. Wang, X. Wang and M. Antonietti, *Angew. Chem., Int. Ed.*, 2012, **51**, 68.
32. X. C. Wang, K. Maeda, A. Thomas, K. Takanabe, G. Xin, J. M. Carlsson, K. Doman and M. A. Antonietti, *Nat. Mater.*, 2009, **8**, 76.
33. S. Cao and J. Yu, *J. Phys. Chem. Lett.*, 2014, **5**, 2101.
34. S. Yang, Y. Gong, J. Zhang, L. Zhan, L. Ma, Z. Fang, R. Vajtai, X. Wang and P. M. Ajayan, *Adv. Mater.*, 2013, **25**, 2452.
35. X. Wang, K. Maeda, X. Chen, K. Takanabe, K. Doman, Y. Hou, X. Fu and M. Antonietti, *J. Am. Chem. Soc.*, 2009, **131**, 1680.
36. J. Hong, X. Xia, Y. Wang and R. Xu, *J. Mater. Chem.*, 2012, **22**, 15006.
37. G. Zhang, J. Zhang, M. Zhang and X. Wang, *J. Mater. Chem.*, 2012, **22**, 8083.
38. Y. Wang, Y. Di, M. Antonietti, H. R. Li, X. F. Chen and X. C. Wang, *Chem. Mater.*, 2010, **22**, 5119.
39. J. Liu, Y. Liu, N. Liu, Y. Han, X. Zhang, H. Huang, Y. Lifshitz, S. T. Lee, J. Zhong and Z. Kang, *Science*, 2015, **347**, 970.
40. X. Wang, X. Chen, A. Thomas, X. Fu and M. Antonietti, *Adv. Mater.*, 2009, **21**, 1609.
41. K. Maeda, X. Wang, Y. Nishihara, D. Lu, M. Antonietti and K. Domen, *J. Phys. Chem. C*, 2009, **113**, 4940.
42. J. D. Hong, Y. S. Wang, Y. B. Wang, W. Zhang and R. Xu, *ChemSusChem*, 2013, **6**, 2263.
43. Y. D. Hou, A. B. Laursen, J. S. Zhang, G. G. Zhang, Y. S. Zhu and X. C. Wang, *Angew. Chem., Int. Ed.*, 2012, **52**, 3621.
44. F. He, G. Chen, Y. Yu, S. Hao, Y. Zhou and Y. Zheng, *ACS Appl. Mater. Interfaces*, 2014, **6**, 7171.
45. S. C. Yan, Z. S. Li and Z. G. Zou, *Langmuir*, 2010, **26**, 3894.
46. L. Y. Huang, H. Hu, Y. P. Li, H. M. Li, X. N. Cheng, J. X. Xia, Y. G. Xu and G. B. Cai, *Dalton Trans.*, 2013, **42**, 8606.
47. K. Katsumata, R. Motoyoshi, N. Matsushita and K. Okada, *J. Hazard. Mater.*, 2013, **260**, 475.
48. C. G. Liu, X. T. Wu, X. F. Li and X. G. Zhang, *RSC Adv.*, 2014, **4**, 62492.
49. L. Lei, H. Jin, Q. Zhang, J. Xu, D. Gao and Z. Fu, *Dalton Trans.*, 2015, **44**, 795.
50. X. X. Wang, L. H. Zhang, H. J. Lin, Q. Y. Nong, Y. Wu, T. H. Wu and Y. M. He, *RSC Adv.*, 2014, **4**, 40029.
51. J. Fu, B. B. Chang, Y. L. Tian, F. N. Xi and X. P. Dong, *J. Mater. Chem. A*, 2013, **1**, 3083.
52. Y. Zhou, L. Zhang, J. Liu, X. Fan, B. Wang, M. Wang, W. Ren, J. Wang, M. Li and J. Shi, *J. Mater. Chem. A*, 2015, **3**, 3862.
53. Y. Li, L. Fang, R. Jin, Y. Yang, X. Fang, Y. Xing and S. Song, *Nanoscale*, 2015, **7**, 758.
54. T. T. Li, L. H. Zhao, Y. M. He, J. Cai, M. F. Luo and J. J. Lin, *Appl. Catal. B: Environ.*, 2013, **129**, 255.
55. L. Q. Ye, J. Y. Liu, Z. Jiang, T. Y. Peng and L. Zan, *Appl. Catal. B: Environ.*, 2013, **142–143**, 1.

56. T. Yan, Q. Yan, X. Wang, H. Liu, M. Li, S. Lu, W. Xu and M. Sun, *Dalton Trans.*, 2015, **44**, 1601.
57. Y. M. He, L. H. Zhang, B. T. Teng and M. H. Fan, *Environ. Sci. Technol.*, 2015, **49**(1), 649.
58. N. Tian, H. Huang, Y. He, Y. Guo, T. Zhang and Y. Zhang, *Dalton Trans.*, 2015, **44**, 4297.
59. L. H. Zhang, X. X. Wang, Q. Y. Nong, H. J. Lin, B. T. Teng, L. H. Zhao, T. H. Wu and Y. M. He, *Appl. Surf. Sci.*, 2015, **329**, 143.
60. Y. J. Sun, W. D. Zhang, T. Xiong, Z. W. Zhao, F. Dong, R. Q. Wang and W. K. Ho, *J. Colloid Interface Sci.*, 2014, **418**, 317.
61. F. Dong, Z. W. Zhao, T. Xiong, Z. L. Ni, W. D. Zhang, Y. J. Sun and W. K. Ho, *ACS Appl. Mater. Interfaces*, 2013, **5**, 11392.
62. S. Choudhury, J. O. Baeg, N. J. Park and R. K. Tadaw, *Green Chem.*, 2014, **16**, 4389.
63. K. Maeda, *ACS Catal.*, 2013, **3**, 1486.
64. K. Sayama, R. Yoshida, H. Kusama, K. Okabe, Y. Abe and H. Arakawa, *Chem. Phys. Lett.*, 1997, **277**, 387.
65. R. Abe, K. Sayama, K. Domen and H. Arakawa, *Chem. Phys. Lett.*, 2001, **344**, 339.
66. R. Abe, T. Takata, H. Sugihara and K. Domen, *Chem. Commun.*, 2005, **30**, 3829.
67. M. Higashi, R. Abe, A. Ishikawa, K. Teramura, B. Ohtani and K. Domen, *Chem. Lett.*, 2008, **37**, 138.
68. R. Abe, K. Sayama and H. Sugihara, *J. Phys. Chem. B*, 2005, **109**, 16052.
69. Y. Miseki, S. Fujiyoshi, T. Gunji and K. Sayama, *Catal. Sci. Technol.*, 2013, **3**, 1750.
70. P. Zhou, J. Yu and M. Jaronec, *Adv. Mater.*, 2014, **26**, 4920.
71. H. Tada, T. Mitsui, T. Kiyonaga, T. Akita and K. Tanaka, *Nat. Mater.*, 2006, **5**, 782.
72. Y. Min, G. He, Q. Xu and Y. Chen, *J. Mater. Chem. A*, 2014, **2**, 1294.
73. Y. M. He, L. H. Zhang, B. T. Teng and M. H. Fan, *Environ. Sci. Technol.*, 2015, **49**(1), 649.
74. Z. Cheng, B. Fan, Q. Liu, Z. G. Zhang and X. M. Fang, *J. Mater. Chem. A*, 2015, **3**, 4652.
75. H. G. Kim, E. D. Jeong, P. H. Borse, S. Jeon, K. Yong, J. S. Lee, W. Lo and S. H. Oh, *Appl. Phys. Lett.*, 2006, **89**, 064103.
76. P. Li, Y. Zhou, H. Li, Q. Xu, X. Meng, X. Wang, M. Xiao and Z. Zou, *Chem. Commun.*, 2015, **51**, 800.
77. Y. Sasaki, H. Nemoto, K. Saito and A. Kudo, *J. Phys. Chem. C*, 2009, **113**, 17536.
78. Q. Jia, A. Iwase and A. Kudo, *Chem. Sci.*, 2014, **5**, 1513.
79. K. J. Vaishnav, S. S. Arbuj, S. B. Rane and D. P. Amalnerkar, *RSC Adv.*, 2014, **4**, 47637.
80. W. Qin, F. Xin, Y. Liu, X. Yin and W. Ma, *J. Colloid Interface Sci.*, 2011, **356**, 257.
81. I. Aslam, C. Cao, M. Tanveer, M. H. Farooq, W. S. Khan, M. Tahir, F. Idrees and S. Khalid, *RSC Adv.*, 2015, **5**, 6019.

82. J. Yu, S. Wang, J. Low and W. Xiao, *Phys. Chem. Chem. Phys.*, 2013, **15**, 16883.
83. Y. M. He, L. H. Zhang, X. X. Wang, Y. Wu, H. J. Lin, L. H. Zhao, W. Z. Weng, H. L. Wan and M. H. Fan, *RSC Adv.*, 2014, **4**(26), 13610.
84. L. Ye, J. Liu, C. Gong, L. Tian, T. Peng and L. Zan, *ACS Catal.*, 2012, **2**, 1677.
85. K. Awazu, M. Fujimaki, C. Rockstuhl, J. Tominaga, H. Murakami, Y. Ohki, N. Yoshida and T. Watanabe, *J. Am. Chem. Soc.*, 2008, **130**, 1676.
86. K. L. Kelly, E. Coronado, L. L. Zhao and G. C. Schatz, *J. Phys. Chem. B*, 2003, **107**, 668.
87. J. J. Mock, M. Barbic, D. R. Smith, D. A. Schultz and S. Schultz, *J. Chem. Phys.*, 2002, **116**, 6755.
88. C. Hu, Y. Lan, J. Qu, X. Hu and A. Wang, *J. Phys. Chem. B*, 2006, **110**, 4066.
89. P. Christopher, D. B. Ingram and S. Linic, *J. Phys. Chem. C*, 2010, **114**, 9173.
90. X. Zhang, Y. L. Chen, R. S. Liu and D. P. Tsai, *Rep. Prog. Phys.*, 2013, **76**, 046401.
91. P. Christopher, H. Xin and S. Linic, *Nat. Chem.*, 2011, **3**, 467.
92. I. Thomann, B. A. Pinaud, Z. B. Chen, B. M. Clemens, T. F. Jaramillo and M. L. Brongersma, *Nano Lett.*, 2011, **11**, 3440.
93. F. Le, D. W. Brandl, Y. A. Urzhumov, H. Wang, J. Kundu, N. J. Halas, J. Aizpurua and P. Nordlander, *ACS Nano*, 2008, **2**, 707.
94. V. Mizeikis, E. Kowalska and S. Juodkazis, *J. Nanosci. Nanotechnol.*, 2011, **11**, 2814.
95. W. B. Hou, Z. W. Liu, P. Pavaskar, W. H. Hung and S. B. Cronin, *J. Catal.*, 2011, **277**, 149.
96. Y. Lu, H. T. Yu, S. Chen, X. Qian and H. Z. Zhao, *Environ. Sci. Technol.*, 2012, **46**, 1724.
97. H. L. Duan and Y. M. Xuan, *Phys. E*, 2011, **43**, 1475.
98. Z. Lin, X. Wang, J. Liu, Z. Tian, L. Dai, B. He, C. Han, Y. Wu, Z. Zeng and Z. Hu, *Nanoscale*, 2015, **7**, 4114.
99. J. J. Chen, J. C. S. Wu, P. C. Wu and D. P. Tsai, *J. Phys. Chem. C*, 2011, **115**, 210.
100. I. Bannat, K. Wessels, T. Oekermann, J. Rathousky, D. Bahnemann and M. Wark, *Chem. Mater.*, 2009, **21**, 1645–1653.
101. A. A. Ismail, D. W. Bahnemann, L. Robben, V. Yarovyi and M. Wark, *Chem. Mater.*, 2010, **22**, 108.
102. Y. Tian and T. Tatsuma, *Chem. Commun.*, 2004, **16**, 1810.
103. A. Furube, L. Du, K. Hara, R. Katoh and M. Tachiya, *J. Am. Chem. Soc.*, 2007, **129**, 14852.
104. S. Mubeen, G. Hernandez-Sosa, D. Moses, J. Lee and M. Moskovits, *Nano Lett.*, 2011, **11**, 5548.
105. Z. Jiang, Q. Ouyang, B. Peng, Y. Zhang and L. Zan, *J. Mater. Chem. A*, 2014, **2**, 19861.

106. L. Z. Dong, Y. M. He, T. T. Li, J. Cai, W. D. Hu, S. S. Wang, H. J. Lin, M. F. Luo, X. D. Yi, L. H. Zhao, W. Z. Weng and H. L. Wan, *Appl. Catal., A*, 2014, **472**, 143.
107. V. P. Dinesh, P. Biji, A. Ashok, S. K. Dhara, M. Kamruddin, A. K. Tyagi and B. Raj, *RSC Adv.*, 2014, **4**, 58930.
108. J. Yang, X. Wang, Y. Chen, J. Dai and S. Sun, *RSC Adv.*, 2015, **5**, 9771.
109. H. Fan, G. Li, F. Yang, L. Yang and S. Zhang, *J. Chem. Technol. Biotechnol.*, 2011, **86**, 1107.
110. M. A. Nawi, A. H. Jawad, S. Sabar and W. S. W. Ngah, *Carbonhydr. Polym.*, 2011, **83**, 1146.
111. S. Yurdakal, B. S. Tek, O. Alagöz, V. Augugliaro, V. Loddo, G. Palmisano and L. Palmisano, *ACS Sus. Chem. Eng.*, 2013, **1**, 456.
112. T. S. Symeonidis, I. Tamiolakis, G. S. Armatasb and I. N. Lykakis, *Photochem. Photobiol. Sci.*, 2015, **14**, 563.
113. T. Jiang, C. Jia, L. Zhang, S. He, Y. Sang, H. Li, Y. Li, X. Xu and H. Liu, *Nanoscale*, 2015, **7**, 209.
114. S. Higashimoto, Y. Nakai, M. Azuma, M. Takahashi and Y. Sakata, *RSC Adv.*, 2014, **4**, 37662.
115. S. Kitano, A. Tanaka, K. Hashimoto and H. Kominami, *Phys. Chem. Chem. Phys.*, 2014, **16**, 12554.
116. H. Wang, J. Zhang, Y. M. Cui, K. F. Yang, Z. J. Zheng and L. W. Xu, *RSC Adv.*, 2014, **4**, 34681.
117. Q. Jia, D. Zhao, B. Tang, N. Zhao, H. Li, Y. Sang, N. Bao, X. Zhang, X. Xu and H. Liu, *J. Mater. Chem. A*, 2014, **2**, 16292.
118. Y. Zhang and Y. J. Xu, *RSC Adv.*, 2014, **4**, 2904.
119. S. Furukawa, A. Tamura, T. Shishido, K. Teramura and T. Tanaka, *Appl. Catal., B*, 2011, **110**, 216.
120. S. Furukawa, T. Shishido, K. Teramura and T. Tanaka, *ChemPhysChem*, 2014, **15**, 2665.
121. L. Zhang, D. Liu, J. Guan, X. Chen, X. Guo, F. Zhao, T. Hou and X. Mu, *Mater. Res. Bull.*, 2014, **59**, 84.
122. F. Su, S. C. Mathew, G. Lipner, X. Fu, M. Antonietti, S. Blechert and X. Wang, *J. Am. Chem. Soc.*, 2010, **132**, 16299.
123. N. Zhang, Y. Zhang, X. Pan, X. Fu, S. Liu and Y. J. Xu, *J. Phys. Chem. C*, 2011, **115**, 23501.